2015

PETROPHYSICAL ANALYSIS AND ROCK-PHYSICS BASED PREDICTION OF SONIC VELOCITIES IN CARBONATES

Yeliz Egemen
Michigan Technological University

PETROPHYSICAL ANALYSIS AND ROCK-PHYSICS BASED PREDICTION OF SONIC VELOCITIES IN CARBONATES

By

Yeliz Egemen

A THESIS

Submitted in partial fulfillment of the requirements for the degree of

MASTER OF SCIENCE

In Geophysics

MICHIGAN TECHNOLOGICAL UNIVERSITY

2015

This thesis has been approved in partial fulfillment of the requirements for the Degree of MASTER OF SCIENCE in Geophysics

Department of Geological and Mining Engineering and Sciences

Thesis Advisor: *Dr. Wayne D. Pennington*

Committee Member: *Dr. Roger M. Turpening*

Committee Member: *Prof. Mir Sadri*

Department Chair: *Dr. John S. Gierke*

Table of Contents

Acknowledgements

First and foremost I would like to thanks to my advisor, Dr. Wayne D. Pennington. It was his guidance, support, and expertise in geophysics that made my research and this paper possible. Furthermore I would like to acknowledge the committee members in my department, Professor Mir Sadri and Dr. Roger Turpening for their support and help.

I also want to recognize the team at Jason (now part of CGG) for the PowerLog software they provided, enabling me to analyze the data necessary to complete my research.

Last but not least are my friends and family. Their support goes beyond words I can express in this acknowledgment. My friends Evan Krettek, Qiang Guo, Lu Yang, Deniz Yener, Fatmanur Karaman, Solmaz Hajmohammadi, Robert Richard and Paniz Khanmohammadi Hazaveh have all helped me both personally and as a graduate student. My family, Selvin, Yesim and Özdemir Egemen, played major roles in carrying me through tough times and always pushing me to do my best.

Abstract

This study performs a petrophysical analysis and rock-physics modeling of the Traverse Formation, using eleven different wells. In the first part of this study, well logs, crossplots, and mineral identification were used to determine the rock components, lithology, and to predict the sonic velocities of carbonate rocks using conventional methods for two of those wells.

In the second part of this study, rock-physics modeling methods were used to predict the sonic velocities using the Kuster-Toksöz equations. Sonic velocities are very difficult to predict in carbonate rock because of their complex pore systems. To overcome this difficulty, multiple aspect ratios for porosity were used to calculate sonic velocities for the limestone, dolomite, quartz, anhydrite, and shale mixtures. Having determined the lithology from conventional log analysis, the matrix moduli and densities were estimated. Then the Kuster-Toksöz equations were used to calculate the elastic properties, using different aspect ratios in an effort to obtain the best estimate for the observed P-wave velocities, and to predict S-wave velocities (which had not been recorded), and compare them with the predicted S-wave from Greenberg and Castagna equations.

1 Introduction

Eleven wells were selected for this study, with appropriate logs covering the Traverse Group Formation in the Michigan Basin, a Middle Devonian carbonate consisting of calcite, dolomite, quartz, anhydrite and shale (Huntoon and Wylie, 2003).

This study attempts to use conventional logs in order to estimate sonic-log values. Carbonate rocks are particularly challenging for such estimates due to the variety and complexity of pore shapes (Xu and Payne, 2009). It is hoped that, through a systematic approach of pore-shape analysis for different mineralogy as determined from conventional logs, improved relations for sonic properties could be obtained. The conventional logs include density (RHOB), neutron-porosity (NPHI, recorded on a limestone scale), gamma-ray (GR), and photo-electric effect (PEF). Four different mineral components were found to occur in the Traverse formation: calcite, dolomite, anhydrite, and quartz. Crossplots of these four logs were used to identify those minerals.

Many empirical relations exist for the prediction of sonic velocities from other information, such as porosity and matrix lithology. These have limited accuracy, and are particularly problematic in carbonate rocks. Sonic velocities depend on many factors other than simple porosity and lithology, including pore type. The Kuster-Toksöz (Kuster and Toksöz, 1974) method assumes that pores can be approximated as penny-shaped ellipsoids of revolution, with aspect ratios representing ranging from fine crack-like pores (between 0.001-0.01) to spherical pores (1.0). Different mineral assemblages tend to exhibit behavior representing

different pore aspect ratios. Other investigators have found certain aspect ratios to be useful in single-lithology rocks (Brie, 1985), and combinations of aspect ratios for mixed lithologies (Xu and White, 1995).

In this study, inspired by the mixed-lithology studies by Xu and White (1995) and Xu and Payne (2009), a complex set of lithologies, including a calcite-quartz mixture, and a dolomite-anhydrite mixture, are analyzed in a systematic manner in an attempt to predict sonic velocities using lithology-dependent pore aspect ratios for the porosity. The first part of this thesis includes a description of the lithology estimate using the eleven wells as examples shown in Appendix 7.1.3. In the second part of this thesis, the Kuster-Toksöz method is used to predict sonic velocities for mixtures found in some of the wells studied.

2 Devonian System Geology

The formation used in this study is found in the Michigan Basin. The Michigan Basin is bounded by the Kankakee Arch, Cincinnati Arch and Findlay Arch (Rupp, 1997). The Devonian System in the Michigan Basin is composed of five formations: Antrim Shale, Traverse Formation, Traverse Limestone, Bell Shale, and Dundee Formation (Lilienthal, 1974). Carbonate and clastic rocks constitute the system with shale in the upper section. The series of intermixed carbonates and clastic rock are due to multiple regression and transgression events in the Middle Devonian (Huntoon and Wylie, 2003).

The uppermost layer of the Devonian System is the Antrim Shale, a dark brown organic shale with a high radioactive response on the gamma-ray log (Lilienthal, 1974; Pringle, 1937). The Antrim Shale has a thickness of 60 ft to 220 ft (Hasenmueller and Bassett, 1979).

The Traverse Formation, Traverse Limestone and Bell Shale make up the Traverse Group. The Traverse Group has a thickness ranging from 80 ft to 900 ft (Huntoon and Wylie, 2003). Traverse Formation is the uppermost layer of the Traverse Group and is composed of gray shale and limestone (Huntoon and Wylie, 2003). The underlying Traverse Limestone is the important formation in this group and consists of dolomite, shale, and anhydrite, with substantial production of gas and oil (Catacosinos et al., 1990). The lowest part of the Traverse Group, the Bell Shale, is a fossiliferous gray shale with thickness of about 80 ft (Huntoon and Wylie, 2003).

The Dundee Limestone underlies the Traverse Group, and is brown to gray limestone with a thickness of 25 ft to 35 ft (Catacosinos et al., 1990; Lilienthal, 1974). If the Bell Shale is not present, then the Dundee directly underlies the Traverse Limestone. This thesis is concerned only with the Traverse Limestone.

3 Methods

Conventional sonic-log prediction can be exemplified by application of a simple sonic-porosity relationship. This will be applied to a few wells, and that prediction compared with recorded sonic values. The technique does not vary with lithology, except for the value of a matrix velocity.

In order to perform more complicated analytical techniques, the lithology of the formation must be known. The eleven wells selected for this study were all logged with the conventional suite of logs (GR, RHOB, NPHI, PEF). In addition, they all had a sonic (DT) log, for comparison with predictions.

Conventional log analysis, including picking of formation tops and crossplot analysis, serves to identify the lithologies to be studied in the Traverse Limestone. Simple predictions of sonic velocity are performed, using conventional approaches. Finally, the Kuster-Toksöz equations are used, with pore aspect ratios determined in a systematic manner, to predict the sonic velocities.

3.1 Picking Formation Tops

This thesis will focus on the Traverse Limestone of the Traverse Group, consisting primarily of limestone, frequently with high dolomite and shale content. For the most part, the Gamma Ray (GR) log was used to pick tops, since the formations all have distinct GR signatures.

The Traverse Group directly underlies the Antrim Shale with its characteristic high radioactivity (more than 150° API). The top of the Traverse Formation is picked where the GR values suddenly drop below 100° API. The Traverse Formation typically has decreasing GR values with increasing depth. The top of Traverse Limestone, below the Traverse Formation, is identified when the GR log values become stable with depth. The top of Bell Shale, beneath the Traverse Limestone, is identified at the depth where the GR log values suddenly increase, but then remain stable with increasing depth. The Dundee Limestone, with extremely low and stable GR values, directly underlies the Bell Shale. An example of logs with the tops picked is provided in Figure 3.1.

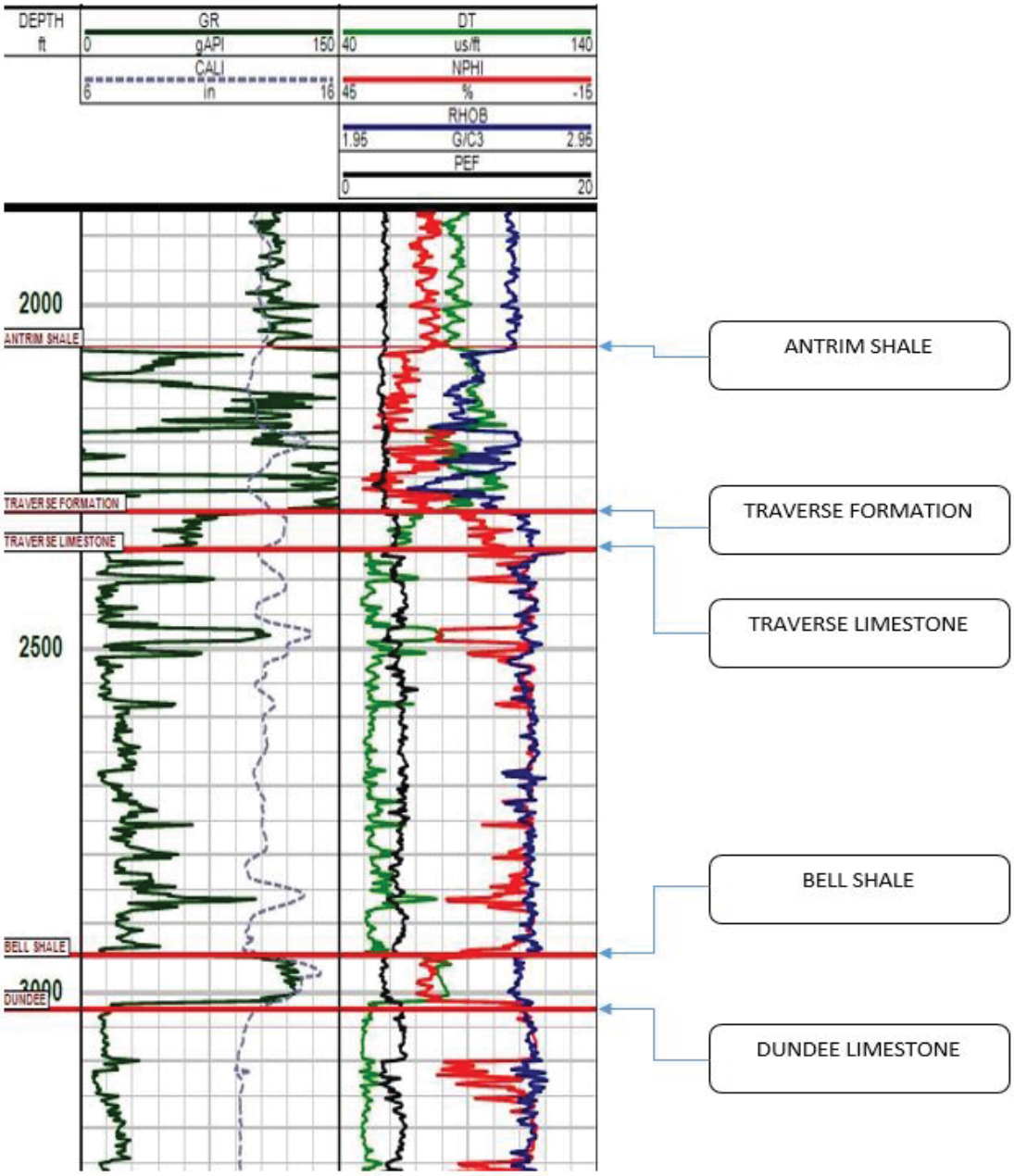

Figure 3.1 An example of the gamma ray (GR), density (RHOB), sonic (DT) and neutron porosity (NPHI) logs, with the tops of the Antrim Shale, Traverse Formation, Traverse Limestone, Bell Shale and Dundee picked in the Consumers Power Co well. This log displays use the following convention: The first column lists the depth, in feet. The first log track includes the GR log in black, and include the caliper (CAL) in dashed grey. The second log track displays the RHOB (blue), NPHI (red), and DT (green) and PEF (black).

3.2 Petrophysical Analysis

The important parameters that determine the sonic velocities are the mineral composition of the rocks and the porosity type; these parameters were estimated with petrophysical analysis. The gamma ray log was used to determine shale content. The density log, neutron log, and photoelectric absorption factor log were used to detect porosity of the rock, calculate the volumetric factor and composition of the other minerals.

Various crossplots which include the Neutron-Density crossplot, the Mineral Identification (MID) of dry grain density (DGA) and photo-electric effect (UMA) crossplot and the Density-Photoelectric Absorption (PEF) crossplot were used to determine lithology. These will be described individually here, with display parameters used in all presentations. This discussion begins with an example of a limestone containing some quartz, using the Martin well and Kennedy wells. The other lithology, present deeper in these wells, consists of dolomite and anhydrite, and will be discussed later using the Kennedy well. These two wells are provided as examples, and the remaining nine wells are presented in an appendix.

The shallower portion of the Traverse Limestone in the Martin well, with logs and crossplots displayed in Figures 3.2.1-4, presents a limestone with a significant amount of quartz typical of many wells. Some parts of the formation also contain a significant amount of clay, but for this example the depths containing clay will be ignored. The logs are displayed in Figure 3.2.1, covering a large depth interval with a range of lithologies (clean limestone shallower and more clay-rich or shalier deeper).

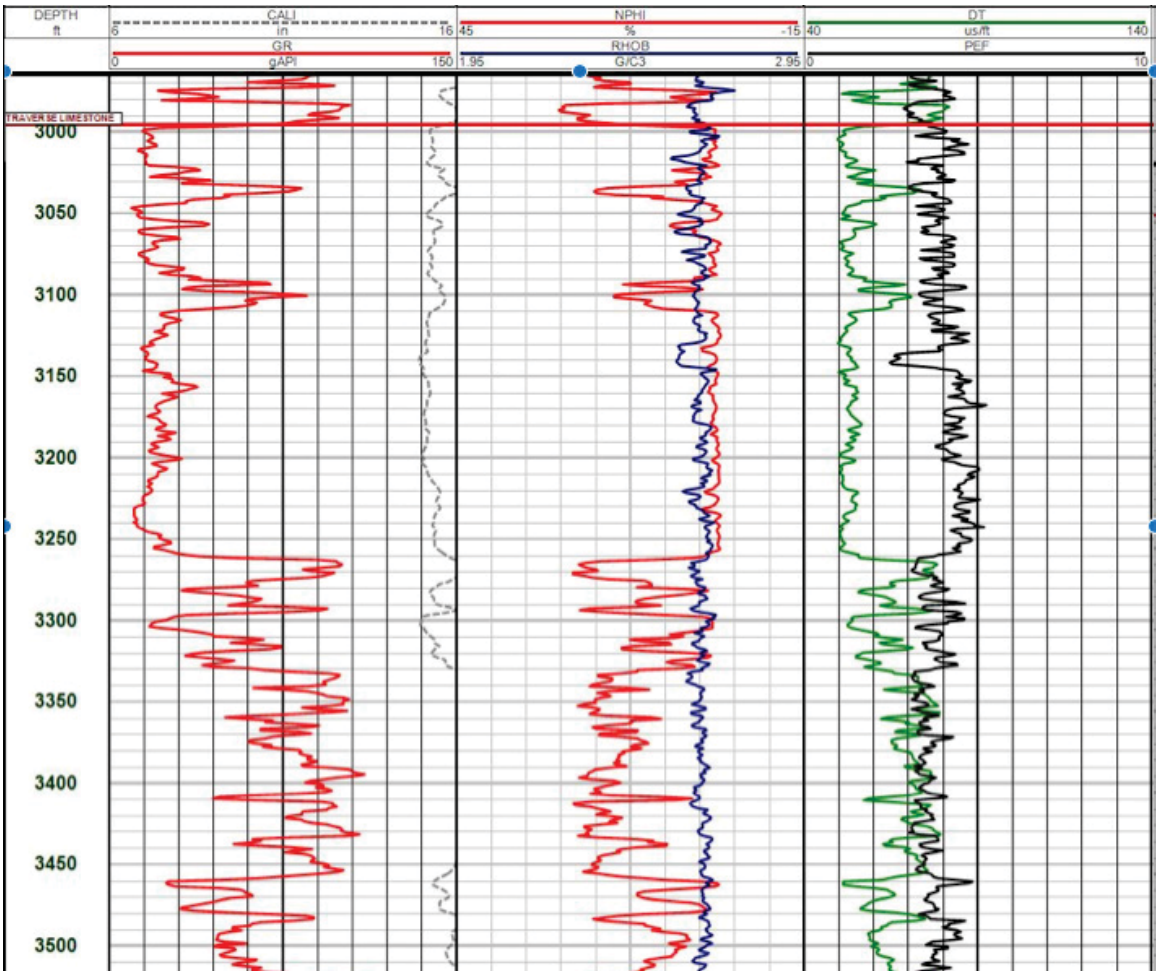

Figure 3.2.1. A log suite for Traverse Limestone in the Martin well, with depth in ft. In the first track, the red line is gamma-ray log, GR, and the grey line is the caliper log, CALI. In the second track the red line is the neutron log, NPHI, the blue line represents the density log, RHOB. Finally, in the third track the green line is the sonic log, DT, and the black line represents the photo-electric factor log, PEF. The various log scales are indicated in the track headers. (The depth range used for crossplots in Figures 3.2.2 - 3.2.4 is 3150-3250 ft).

In all of the wells studied, combinations of four logs, the gamma ray log, density log, neutron log, and photoelectric absorption factor log were used to identify the five mineral components: quartz, calcite, dolomite and anhydrite (the fifth constraint is that the sum of their components must equal one, a feature exploited by the crossplots). Figure 3.2.2 shows a typical neutron-density crossplot, with the color axis showing shale content (from GR

log), over a depth range that includes the limestone with quartz (3150-3250 ft). This crossplot suggests that in this well, the Traverse Limestone includes not only limestone, but also a significant amount of quartz and a small amount of clay. The mineral identification "MID" crossplot of UMA and DGA in Figure 3.2.3 uses dry grain density (DGA or RHOMAND), determined from RHOB and NPHI, and the photo-electric effect (UMA or UMAP), determined from PEF and RHOB, to help estimate the mineral components. The RHOB-PEF crossplot shown in Figure 3.2.4, also provides an estimate of mineral composition. Together, the three crossplots yield a reliable estimate of lithology. For the Martin well, with its simple lithology, all three crossplots yield similar results, providing support to the interpretation that in this depth range the formation consists of limestone (LS) with some quartz (labeled SS for sandstone on some plots). Note that in this case, the RHOB-PEF crossplot could be interpreted as suggesting that the rock is either a mixture of limestone and porous dolomite or a mixture of limestone and quartz; the MID crossplot of UMA and DGA removes that ambiguity about dolomite.

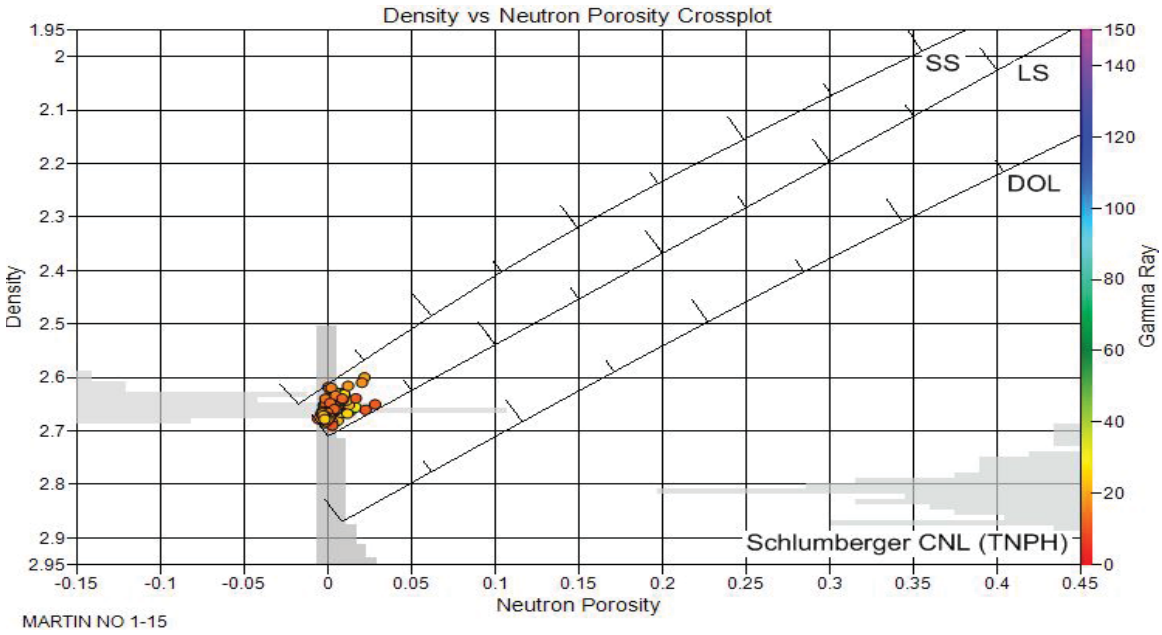

3.2.2 Neutron porosity-Density crossplot of the clean limestone section of the Martin well indicating limestone with quartz. The color bar shows the gamma ray log. Each data point is a different depth in the Traverse Limestone. As is the convention for petrophysical displays, this and other crossplots in this report show the density (RHOB), or the dry grain density (RHOMAND) on the vertical axis, with density values in decreasing order.

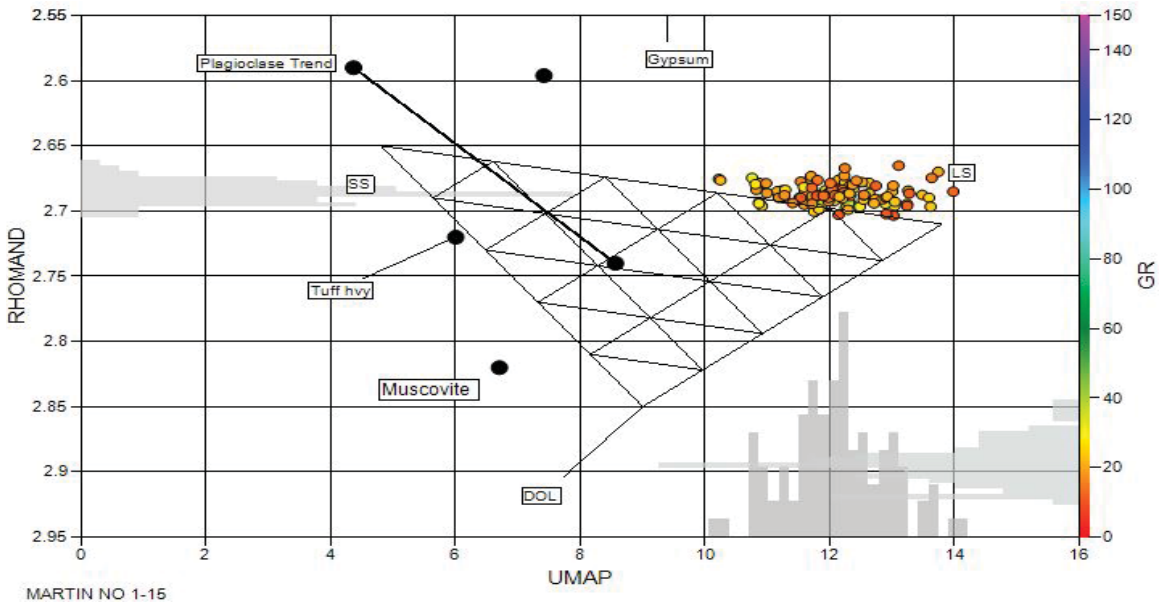

Figure 3.2.3. Mineral identification (MID) crossplot of UMA and DGA of the clean limestone portion of the Martin Well indicates limestone with quartz. The color bar in this crossplot shows the GR log of each data point.

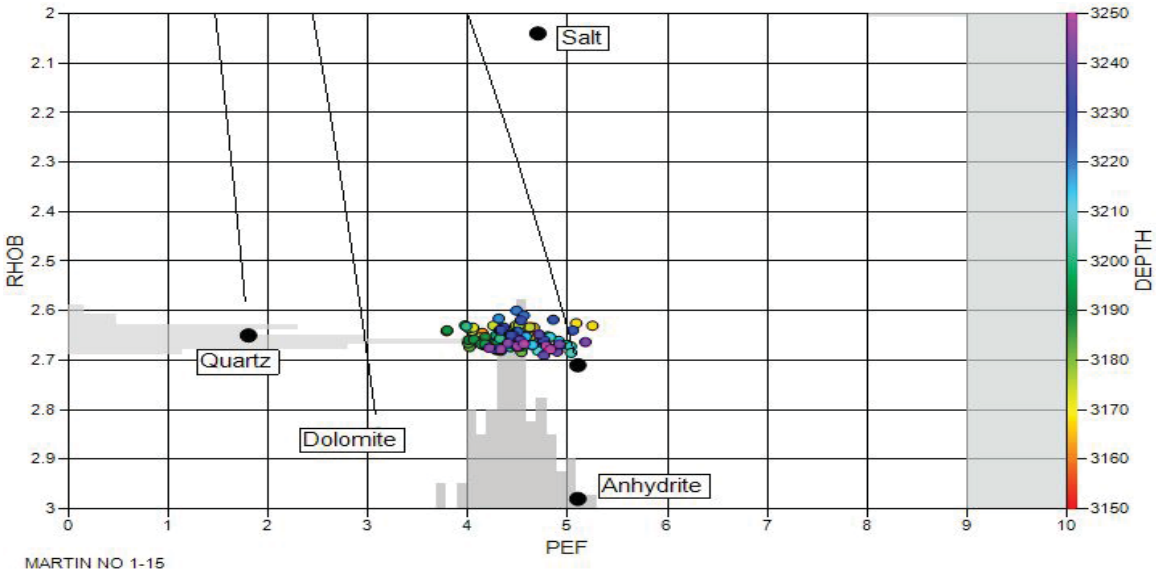

Figure 3.2.4 Density-PEF crossplot of the clean limestone portion of the Martin Well indicates limestone with quartz, although without the other crossplots, this one could be interpreted as limestone with dolomite. The color bar shows depth.

The next example is taken from the Kennedy well, which shows two different results at different depth ranges. The shallower layer is a limestone with a significant amount of quartz and the deeper one is a dolomite with anhydrite. The log in Figure 3.2.5 displays the Traverse Limestone that contains both lithologies.

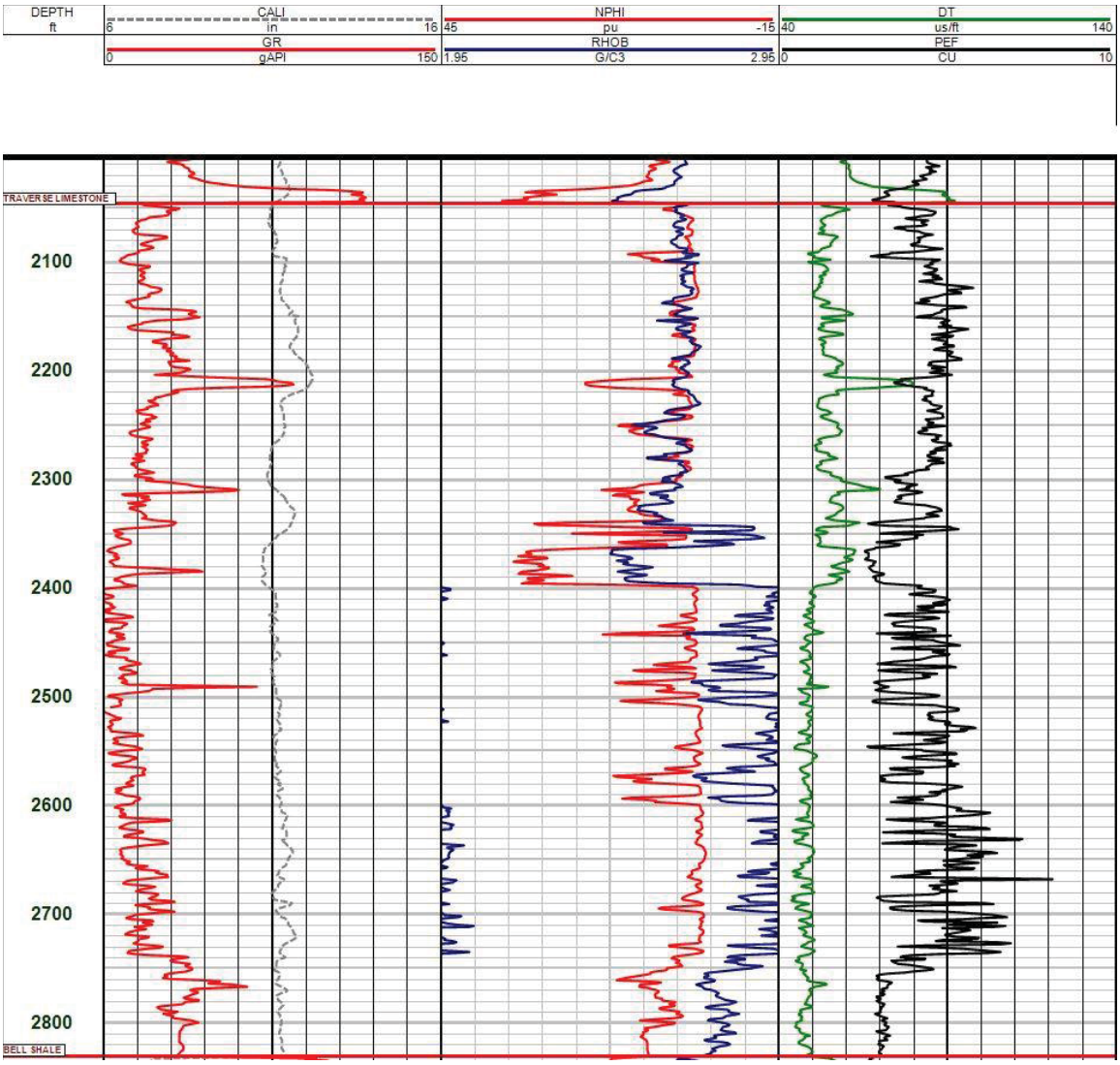

Figure 3.2.5. A log suite for the Kennedy well. Shallower than 2400 ft the lithology is predominantly limestone with quartz, and deeper than 2400 ft it is dolomite with anhydrite.

The first results are represented by the crossplots shown in Figures 3.2.6-8, each using a depth range depth range of 2100 – 2200 ft. All three of the crossplots clearly illustrate that this depth section of the well contains limestone with a significant amount of quartz.

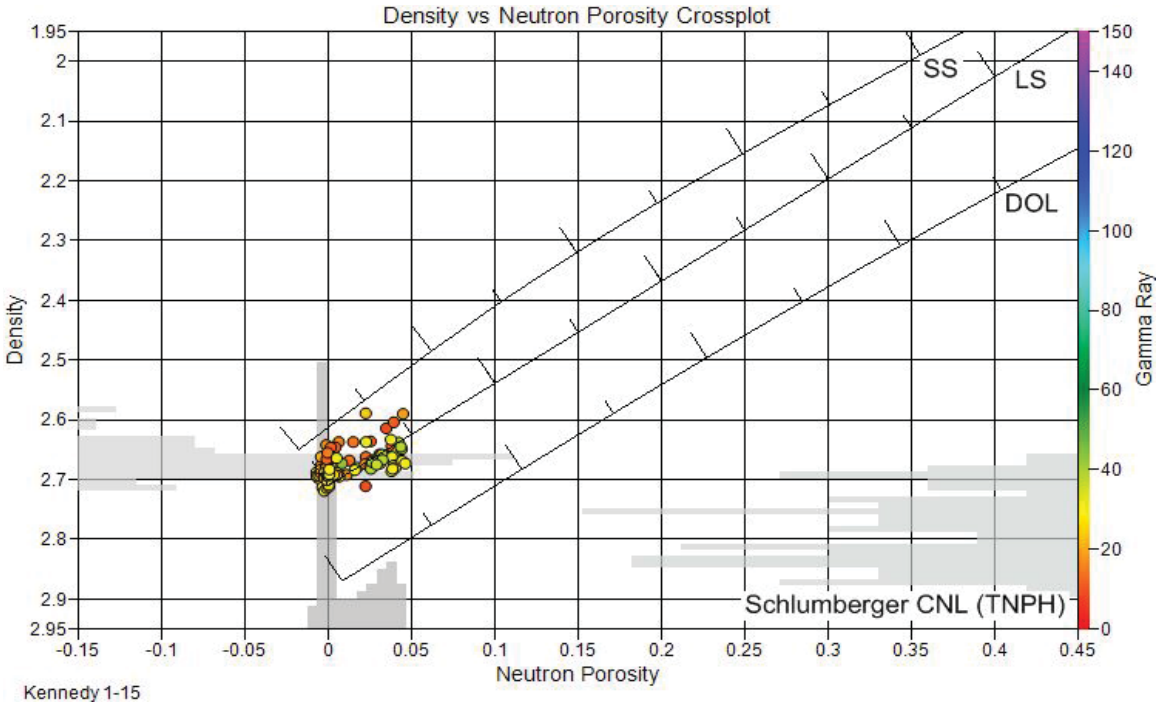

Figure 3.2.6. Density and Neutron porosity crossplot of the Kennedy well, showing limestone and quartz.

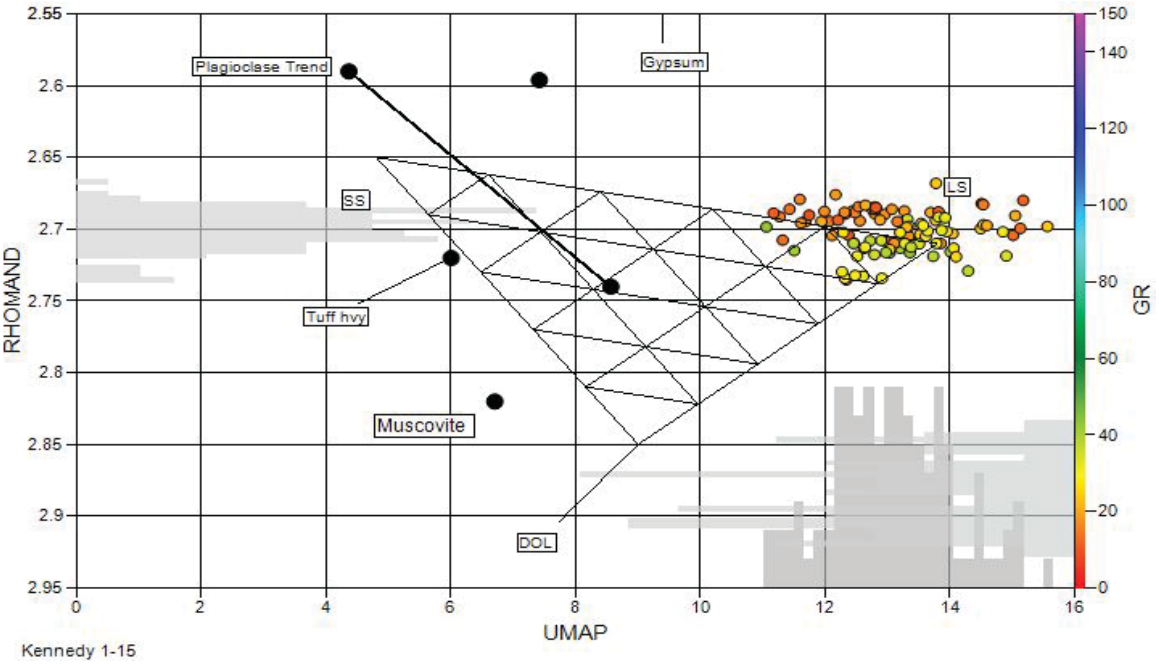

Figure 3.2.7. MID crossplot of UMA and DGA of Kennedy well illustrates the presence of limestone and quartz.

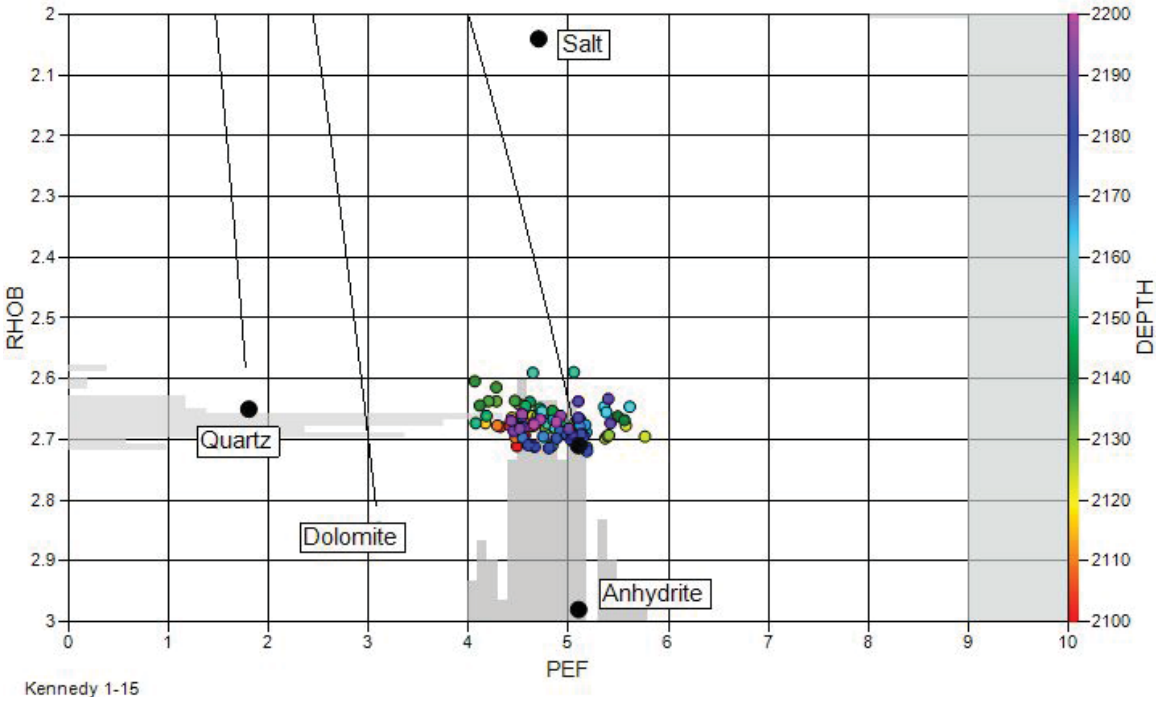

Figure 3.2.8. Density-PEF Crossplot of Kennedy well indicates calcite and quartz. The color bar presents the range of the depth in ft.

The deeper zone of the Kennedy well shows an appreciable amount of dolomite and anhydrite. This is unlike the shallower result, which shows calcite and quartz. Figures 3.2.9-11 show the crossplots for the depth range of 2400-2700 ft. A detailed view of the log of this well can be seen above in the lithology log (Figure 3.2.5).

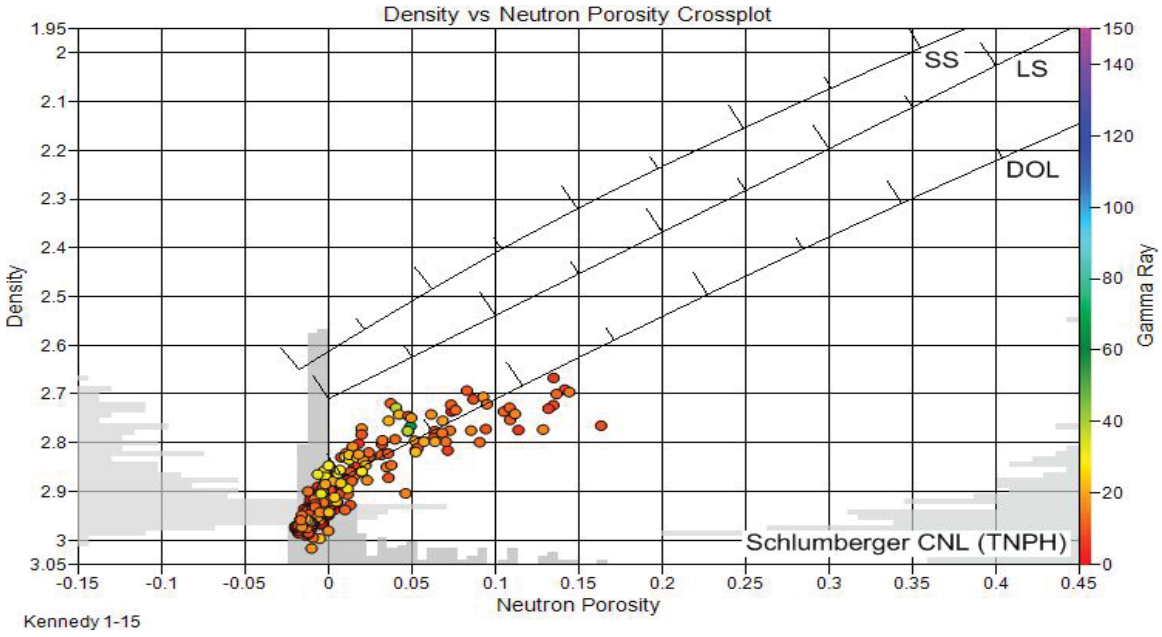

Figure 3.2.9. Neutron porosity-Density crossplot of deeper portion of the Kennedy well suggests dolomite and anhydrite, but the interpretation from this plot alone is not unique.

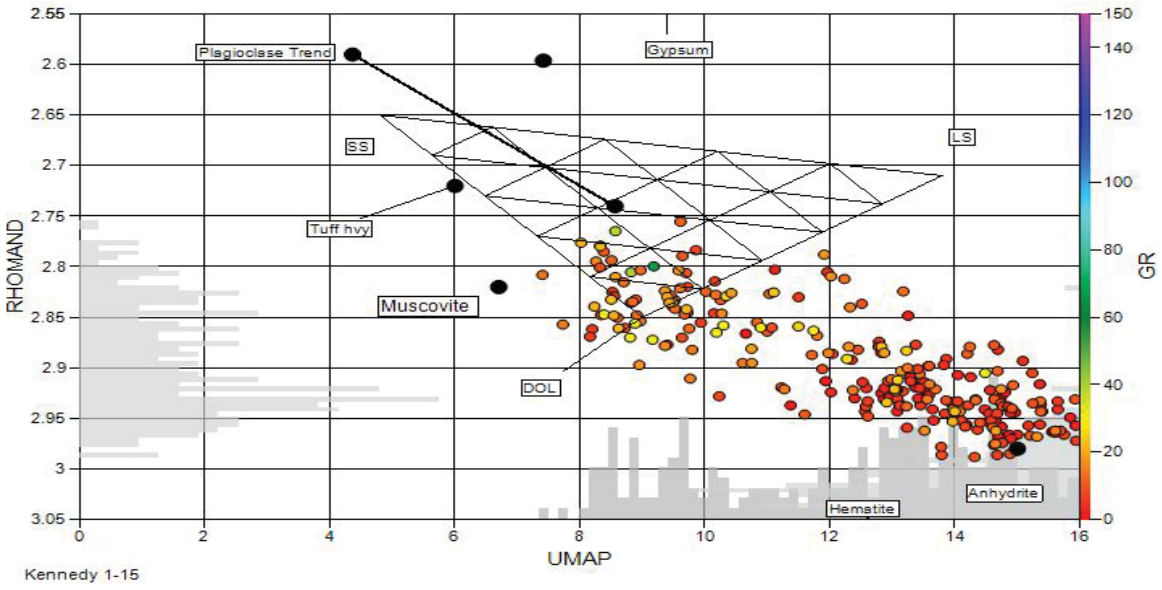

Figure 3.2.10. MID Crossplot of UMA and DGA of Kennedy well indicates dolomite and anhydrite. In this case, the MID plot does not, by itself, indicate the presence of anhydrite, and is non-unique.

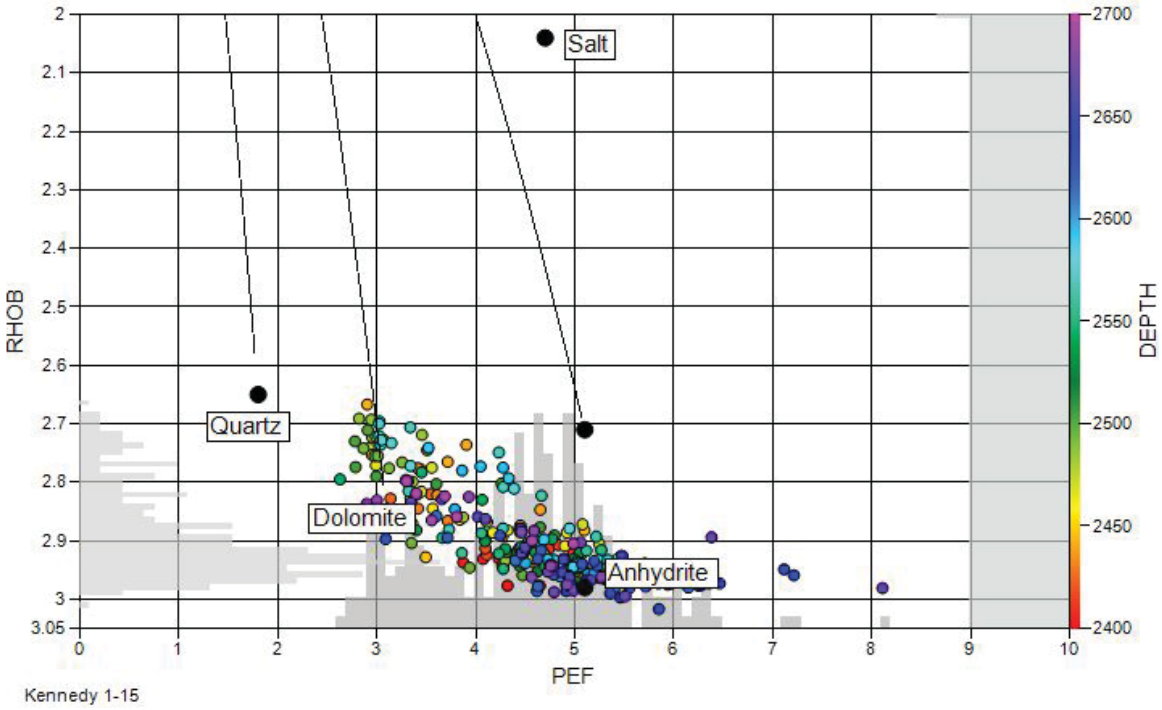

Figure 3.2.11.Density-PEF Crossplot of Kennedy indicate dolomite and anhydrite. This plot clearly indicates that the mineral combination is dolomite and anhydrite, and together with the other crossplots, the ambiguity is essentially eliminated.

3.3 Velocity Determinations

3.3.1 P-wave Velocity Determination from Wyllie's Time-Average Equation

Wyllie's Time-Average Equation (Wyllie et al., 1956) is used to estimate the P-wave transit time using an estimate of porosity. A determination of lithology as described in the previous section, an estimate of porosity from averaging the porosity logs, and the assumption of full saturation with slightly brackish water are used to predict the sonic log. The following form of the equation is used to predict the sonic log;

$$\Delta t = (\Delta t_q * V_q + \Delta t_c * V_c + \Delta t_d * V_d + \Delta t_a * V_a + \Delta t_s * V_s) * (1 - \Phi) + \Delta t_f * \Phi \qquad (1)$$

$\Delta t, \Delta t_q$, Δt_c, Δt_d, Δt_a, Δt_s, and Δt_f are, respectively, Travel Times (slownesses) of the bulk rock and the matrix components quartz, calcite, dolomite, anhydrite, clay and the fluid. V_q, V_c, V_d, V_a and V_s are the fractional volume of the quartz, calcite, dolomite, anhydrite and clay with respect to the total fractional volume. Φ is total porosity.

The slowness of each mineral is presented in Table 3.3.1 (Pirson, 1983). The fractional volumes (V) of the minerals were calculated from the crossplots. In the following section, Figure 3.3.3.2 shows the P-wave velocity obtained from Wyllie's Time-Average equation. The predicted P-wave velocity was more accurate in limestone than in layers containing significant shale or the dolomite zone; where there is shale or dolomite content in the Traverse formation, the difference between the P-wave velocity observed and the P-wave velocity from Wyllie's Time-Average equation increases.

Table 3.3.1 The matrix travel time of each mineral; subscripts used in Equation 1.

Mineral (subscript)	Quartz (q)	Calcite (c)	Anhydrite (a)	Dolomite (d)	Clay (s)	Water (f)
Travel Time Slowness (Δt) ($\mu sec/ft$)	56	49	50	44	85	189

3.3.2 S-wave Determination from Greenberg and Castagna

Shear-wave velocity estimation is also important in seismic interpretation to predict bright spots or other attributes. Greenberg and Castagna developed a method to predict shear wave velocity using lithology and porosity and assuming full water saturation (Greenberg and Castagna, 1992). The following equation shows the relationship between shear wave (S-wave) velocity and compressional wave (P-wave) velocity dependent on the lithology. Table 3.3.2. presents the regression coefficients for predicting the S-wave velocity from the P-wave velocity for the various lithologies (Greenberg and Castagna, 1992).

$$VS= (VP^2 * a_1 + VP * a_2 + a_3) *V_q + (VP^2 * a_1 + VP * a_2 + a_3) *V_c + (VP^2 * a_1 + VP * a_2 + a_3) *V_d + (VP^2 * a_1 + VP * a_2 + a_3) *V_a \quad (2)$$

Where VS is S-wave velocity, VP is P-wave velocity, and a_1, a_2, and a_3 are regression coefficients for S-wave velocity and P-wave velocity.

Table 3.3.2. The regression coefficients (when velocities are in km/s) for P-wave and S-wave velocities in pure porous matrix

Lithology	Sandstone	Limestone	Dolomite	Shale
a_1	0	-0.05508	0	0
a_2	0.80416	1.01677	0.58321	0.76969
a_3	-0.85588	-1.03049	-0.07775	-0.86735

Figure 3.3.3.2 shows the results of the S-wave velocity predictions from Greenberg and Castagna as well as the results of the Kuster-Toksöz model, which will be discussed in the next section. The relationship between P-wave and S-wave velocities helps to identify lithology, but in this study, since no S-wave logs were recorded, it is not useful for lithology identification.

3.3.3 Velocity Determination from Rock Physics Modeling

Predicting sonic velocities in carbonate rocks is complicated. Xu and White (1995) developed a method of estimating compressional and shear-wave velocities in shaly and clean sandstone using porosity (Xu and Keys, 2002). The Xu and White (1995) method depends on the effect of clay content and the pore aspect ratios for the porosities associated with clays and sands on velocity (Xu and Keys, 2002). The Xu and White (1995) method estimates dry rock bulk moduli from the Gassmann equation (Gassmann, 1951) and shear moduli for the mixture of sand by applying the effective medium method of the Kuster-Toksöz (1974) model (Xu and Keys, 2002). Porosity and pore aspect ratio are the two major factors in this model. The aspect ratio of a pore depends on the effects of clay,

cementation and pressure. Effective pressure affects the closure of the cracks when the gaps have a low aspect ratio (Xu and Keys, 2002). A relationship between elastic properties and lithology types was found when testing different aspect ratios of pores in carbonate rocks for calcite, dolomite, and quartz components.

The Xu-White method relies on the gamma ray responses and porosity determination. Inspired by the Xu-White method, this study applied a similar approach to the Traverse Limestone. The Gassmann equation was not applied to find dry-rock values, as the Xu-White method requires, but instead the method used here simply assumed water-saturated properties. First, I analyzed rocks that had been determined to contain a mixture of limestone and quartz. Eventually, more-complex lithologies were considered, including dolomite and anhydrite. In these examples, I sought the pore aspect ratio that provided predictions of DT that fit the observed logs best (in an RMS sense). The minimum Root Mean Square (RMS) error, shown in Appendix 7.2, was found by searching through a reasonable range of pore aspect ratios and comparing the P-wave velocity predicted with that which was observed by the DT log. By starting with limestone with quartz, and gradually adding complexity in the form of other lithologies, I was able, incrementally, to obtain pore aspect ratios for the additional lithologies.

The mixture properties of bulk modulus and shear modulus were calculated using a volume-weighted average according to the volume fractions of the components (the Voigt average for moduli). The bulk modulus and shear modulus of the matrix minerals are given in Table 3.3.3. (Mavko et all, 2009). The portion of the total porosity assigned to the quartz,

calcite, anhydrite, and dolomite components were computed using their volume fractions (Appendix III), obtained in this study (for simplicity) from crossplots. The total porosity equals the sum of the porosities of quartz, calcite, anhydrite, and dolomite. The porosity of the clay fraction is almost zero, which is why the aspect ratio of the clay was not an important factor. Because of this, the clay in the formation was ignored for the calculations.

Table 3.3.3. The modulus for the matrix and fluid content used in the Kuster-Toksöz modeling performed in this study.

Mineral	Calcite	Quartz	Anhydrite	Dolomite	Fluid
Bulk modulus (GPa)	70	37	56	80	2.4
Shear Modulus (GPa)	30	32	29	45	0

For example in the Martin well, only calcite and quartz components were applied in the clean limestone section of the well. I obtained a predicted DT value for each depth point, based on the porosity at that point, first using a range of values for the aspect ratio for the porosity associated with calcite, and then for that of quartz, until all aspect ratios from 0.001 to 0.2 (with an increment of 0.001) were covered for both types of porosity. In each case, I compared the predicted DT with the observed DT at each depth, and then computed the RMS value of the errors over the depth interval representing the calcite and quartz. The lowest RMS value was found for aspect ratios of calcite using 0.053 and quartz using 0.09. Figure 3.3.3.1 shows the range of RMS errors as a function of pore aspect ratio for the

Martin well while holding first one aspect ratio at its best value, then the other aspect ratio at its best value. We can see in the figure that the aspect ratio of calcite that gives the smallest RMS error is between 0.04 and 0.06 and the aspect ratio of quartz that gives the smallest RMS error is between 0.07 and 0.1. However, the RMS error in each case is not strongly affected by the aspect ratio because the porosity is very small everywhere.

Figure 3.3.3.2. displays the logs for the predicted P-wave velocity (using the technique described here) and the P-wave velocity computed from the Wyllie Time-Average Equation for comparison with the observed P-wave velocity from the DT log. It also shows the S-wave velocity calculated from the approach described here, for comparison with that obtained by the Greenberg and Castagna approach (recall that no S-wave logs were available). The P-wave velocity prediction from the Kuster-Toksöz model gives a better fit to the observed P-wave velocity than that calculated using the Wyllie Time-Average Equation. The mineral fractions were calculated for the predictions as shown in Appendix III.

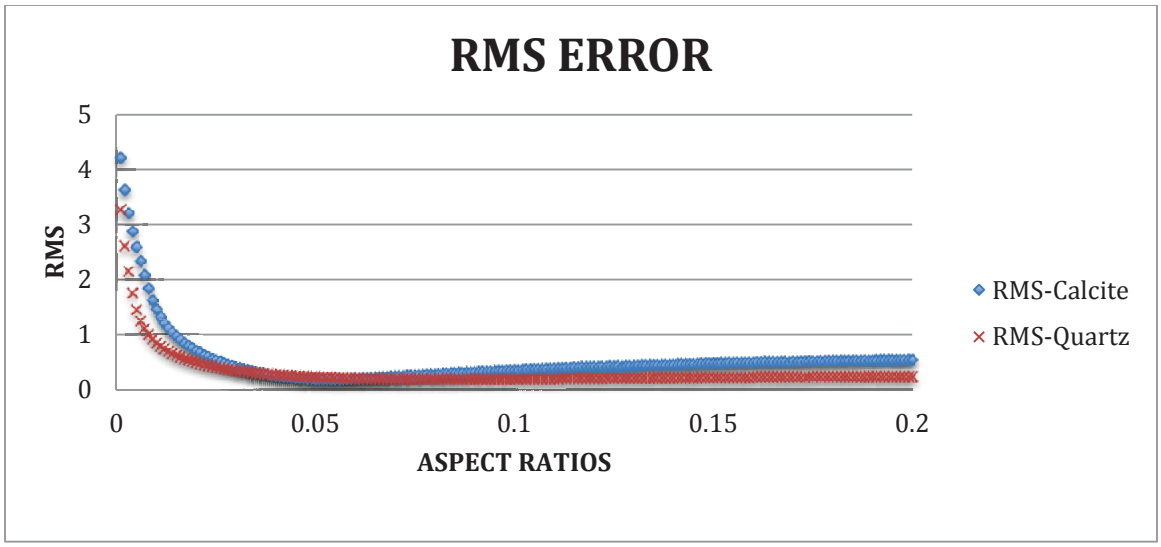

Figure 3.3.3.1. Modeling results for the Martin well. The blue points show the RMS values for a range of aspect ratios for the porosity associated with calcite, from 0 to 0.2, while holding the quartz aspect ratio constant at the value that gives the lowest RMS error. The red points show the RMS values for the a range of aspect ratios for the porosity associated with quartz, from 0 to 0.2, while holding the calcite aspect ratio constant at the value that gives the lowest RMS error.

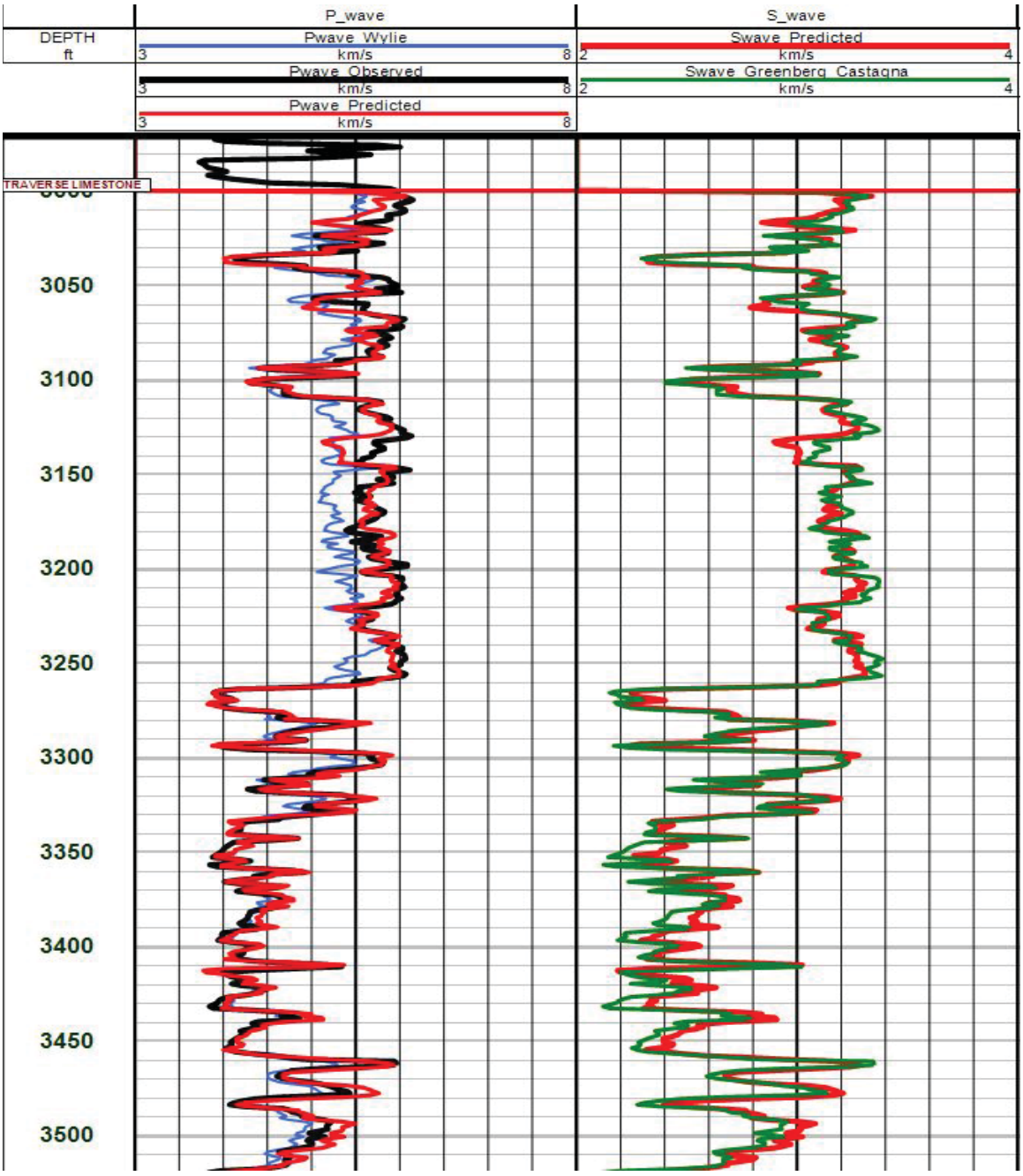

Figure 3.3.3.2. The log displays for Traverse Limestone in the Martin well, the P-wave velocity observed (black line), P-wave velocity predicted using Wyllie's Time Average equation (blue line), and P-wave velocity predicted using Kuster-Toksöz method (red line) in the first track. The second track shows the S-wave velocity (green line) using the Greenberg and Castagna equation and the S-wave velocity predicted (red line) using Kuster-Toksöz method.

While for the Martin well, I only applied the calculations to the depth interval containing limestone (calcite) and quartz, in the Kennedy well I performed two different analyses – one for the calcite/quartz depth range and another one for the dolomite/anhydrite depth range. For the example of a calcite and quartz mixture in the Kennedy Well, over the depth range of 2050-2310 ft, the same technique was used as described above for the Martin well. The shale volume and the shale porosity were insignificant, and so these values did not affect the clay aspect ratio. Where the formation presents a small amount of clay the RMS error increases, which demonstrates the importance of the clay effect. I divided the calcite/quartz portion of the well into small depth ranges grouped according to the observed mineral fractions of calcite and quartz from crossplots, again predicting DT and comparing it with the observed DT at each depth. The RMS values of the errors over the depth range of 2050-2310 ft were calculated as before. The lowest RMS errors obtained were from calcite and quartz pore aspect ratios with values of 0.05 and 0.025, respectively.

Figure 3.3.3.3 shows the range of RMS errors as a function of pore aspect ratio. In this figure, we can clearly see that the value of the aspect ratio of the porosity associated with calcite is fairly tightly constrained (at roughly 0.04); however for the porosity associated with quartz the aspect ratio does not affect the RMS error much, apparently because the porosity associated with the quartz is so small. Comparing Figures 3.3.3.1 and 3.3.3.3, the impact that the larger porosity of the Kennedy well has on the importance of the aspect ratio for calcite becomes apparent. The distinct minimum in the RMS error seen in Figure 3.3.3.3 is in contrast to the relatively flat curve seen in Figure 3.3.3.1.

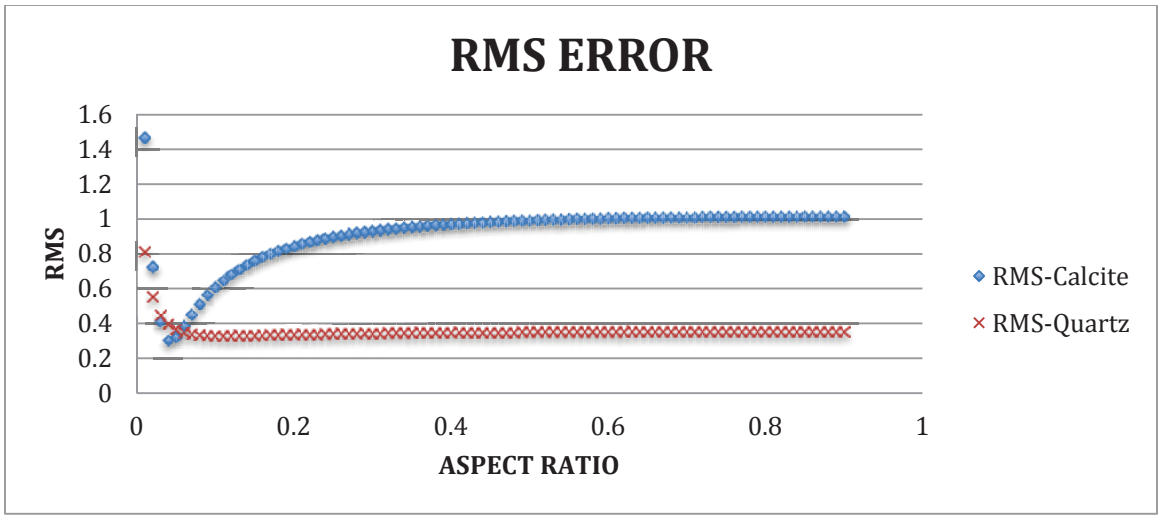

Figure 3.3.3.3. The scatter plot shows that in the blue line the RMS error changes with the range of calcite's aspect ratios while holding the quartz's aspect ratio constant and in the red line the RMS error changes with different range of aspect ratio of quartz while holding the calcite aspect ratio constant at it is best value that gives the lowest RMS error in Kennedy well.

The model for the deeper portion of the Kennedy well uses dolomite and anhydrite components, over a depth range of 2310-2750 ft. There is assumed to be no porosity associated with the anhydrite fraction. Still, the dolomite pore aspect ratio does not significantly affect the RMS error for this depth because there is almost no porosity in the bulk rock throughout this depth range. Figure 3.3.3.4 displays the RMS errors of the pore aspect ratio.

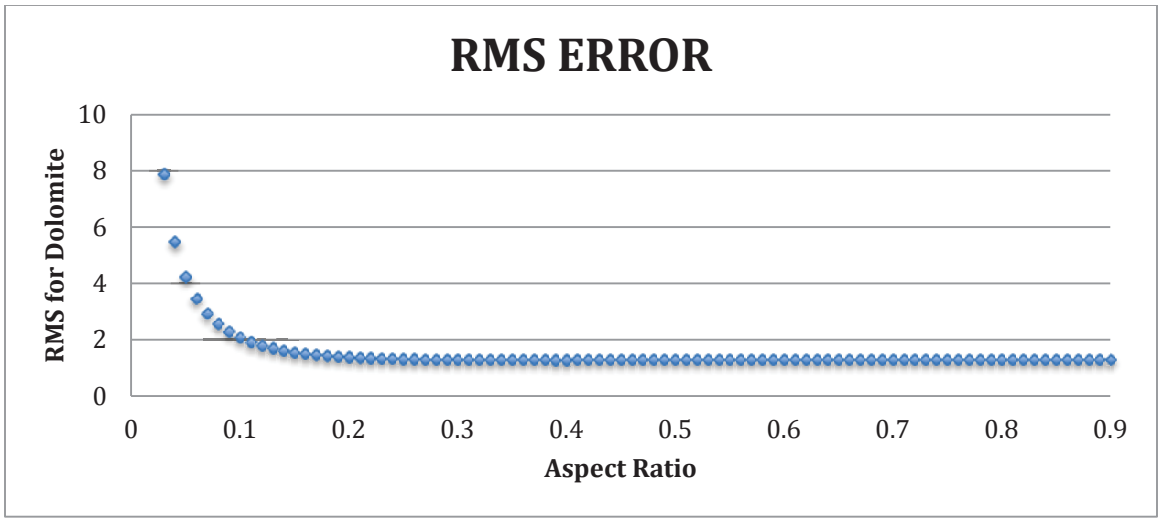

Figure 3.3.3.4. This scatter plot shows the RMS error changes with different aspect ratios of dolomite porosity in the Kennedy well with depth range of 2310-2750 ft.

In Figure 3.3.3.5, the observed P-wave velocity was compared with the result that was obtained using the time-average equation and that predicted using the pore-aspect ratios found to best fit the compressional wave velocity, all shown in the first track. In this figure, the second track displays the S-wave velocity obtained from the Kuster-Toksöz method and that from the Greenberg-Castagna equation. The lithology log that I interpreted using the mineral fractions was calculated from the MID crossplot of UMA and DGA and is described in Appendix III with an enlarged example of the small interval of the depth.

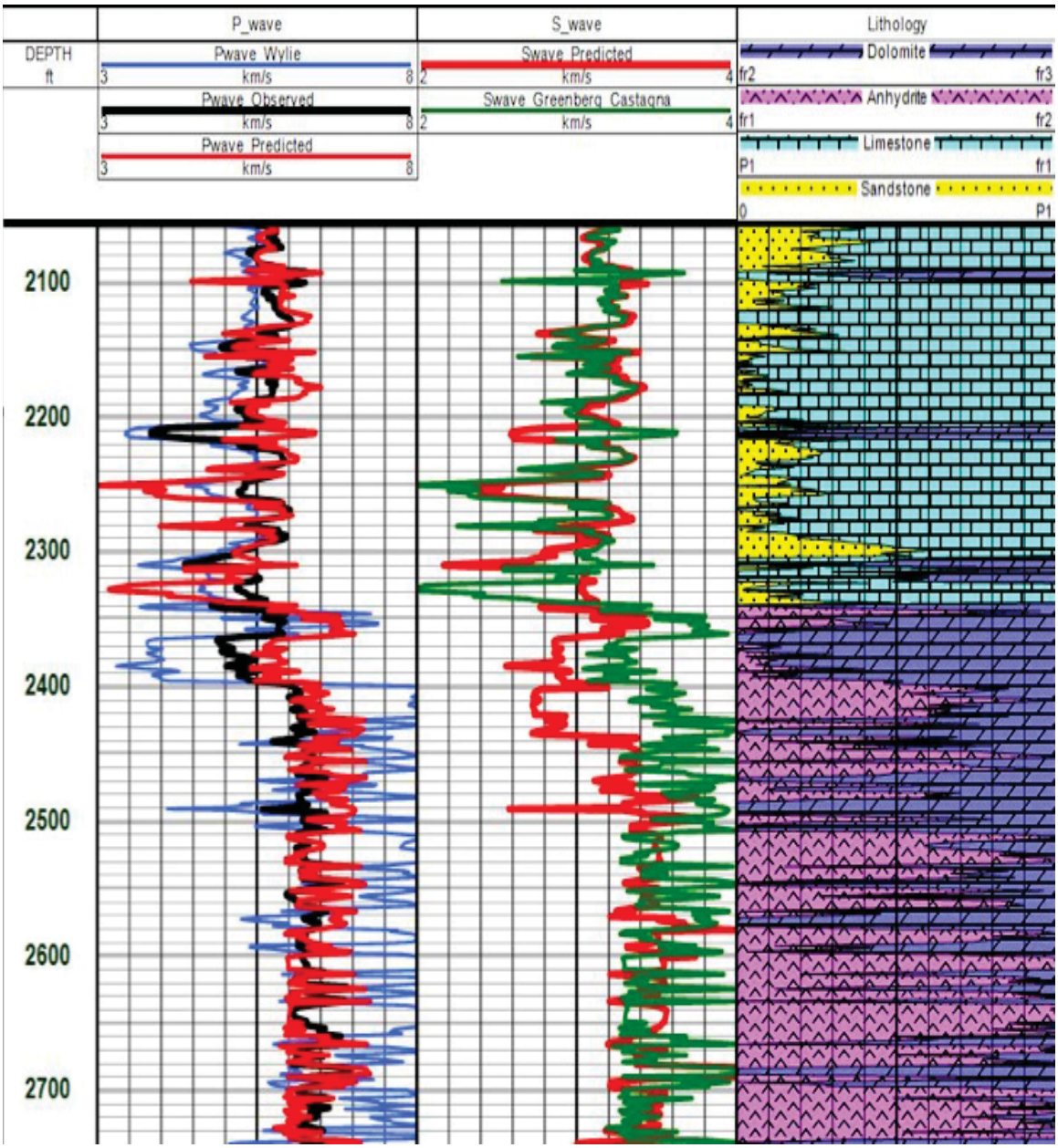

Figure 3.3.3.5. The log of the Kennedy well with Traverse Limestone where limestone and quartz are present in 2050-2310 ft range and anhydrite and dolomite are present in the 2310-2750 ft depth range (also some between 2090-2260 ft). In the first track, the black line is observed P-wave velocity, the red line displays the predicted P-wave velocity obtained from Kuster-Toksöz and the blue line is P-wave velocity obtained from Wyllie's Time Equation. In the second track, the red line shows the predicted S-wave velocity obtained from Kuster-Toksöz, and the green line shows the S-wave velocity obtained from Greenberg and Castagna equations. The third track displays the lithology using the method described in the Appendix III.

3.4 Pore-type classification

There have been other attempts to compare porosities with velocities in an attempt to determine pore shapes. Here I examine one that uses the measured P-wave velocity and the total porosity for clean carbonates.

This study used the Xu and Payne (2009) method to classify the pore types, employing three different pore types similar to the Wang (1991) model (Xu and Payne, 2009). A carbonate rock displays several different types of pores such as moldic, interparticle, and microcracks, and these can be related to porosities and velocities.

The elastic properties are assumed to be homogenously distributed throughout the rock. Typically, moldic pores can be described as round and make the rock stronger than an equivalent porosity with flatter pores. In addition, the velocity is usually higher when the pores are interparticle. Microcracks, in contrast, are generally flat and make the rock weaker with a lower velocity (Xu and Payne, 2009).

Wang et al. (1991), demonstrated the usefulness of a reference line for identifying the effect of pore types on the P-wave velocity, using laboratory data. This result is used here as two different reference lines for the dolomite and limestone regions by applying the same technique to the P-wave velocity of dolomite, which is faster than P-wave velocity of limestone. The reference line by Wang et al. separates the two regions at the relationship identified by an aspect ratio of 0.15. The moldic pores are represented by ratios between 0.15-0.8, the aspect ratio of the interparticle pores is assumed to lie directly on the reference

line of 0.15, and the aspect ratios of the microcrack pore fall between 0.02-0.15 (Wang et al., 1991). In the plots, the moldic pores lie above the reference line, the cracks below it, and the interparticle pores lie directly on the reference line.

From the relationship between porosity and P-wave velocity obtained from Kuster-Toksöz equation for calcite and quartz in the Kennedy well in figure 3.3.3.6, we can see that almost all the P-wave velocities are below the reference line, indicating microcrack pores. In Figure 3.3.3.7 the majority of the relationship between P-wave velocity and porosity is also in the lower limit of the reference line, which similarly shows microcracks.

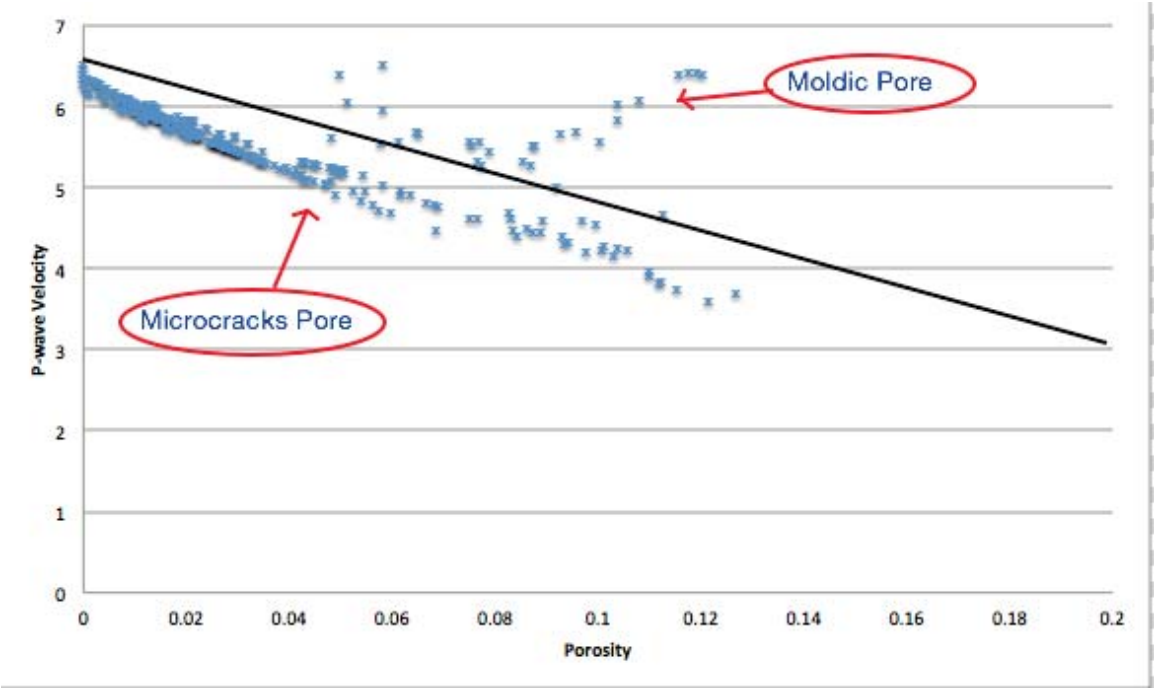

Figure 3.4.1 The relationship between P-wave velocity estimated from Kuster-Toksöz equation and porosity, showing the pore types of a calcite-quartz mix in the Kennedy well. The black line shows the reference line for limestone which refers to be the aspect ratio of 0.15 demonstrated by Wang et al. (1991)

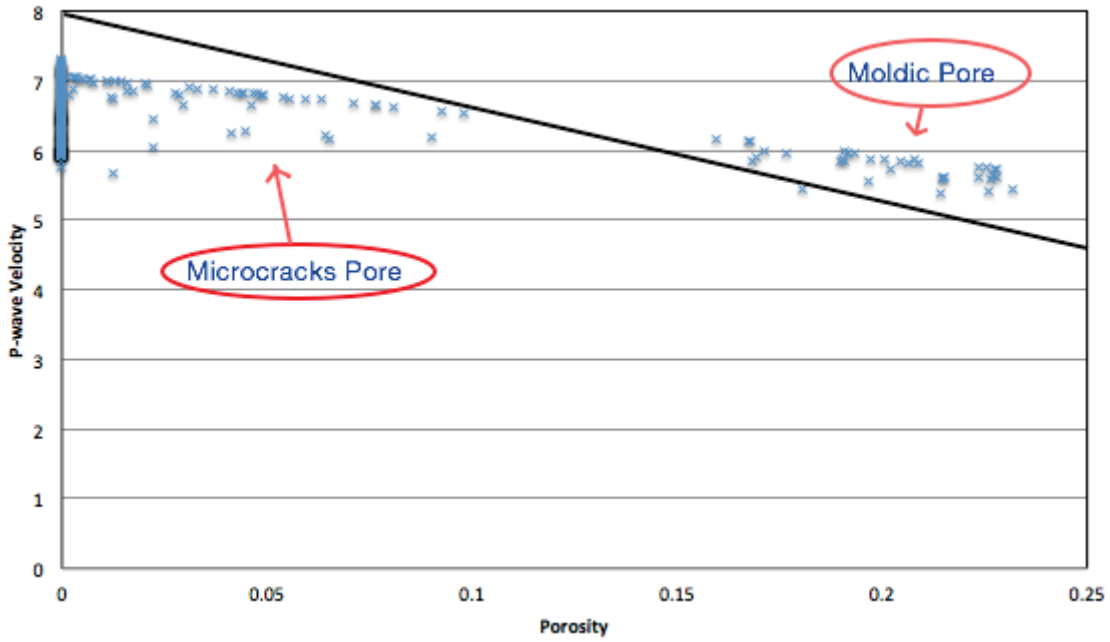

Figure 3.4.2. The relationship between P-wave velocity estimated from Kuster-Toksöz equation and porosity, showing the pore types of a dolomite-anhydrite mix in the Kennedy well. The black line shows the reference line for dolomite which refers to be the aspect ratio of 0.15 demonstrated by Wang et al. (1991)

4 Results & Discussion

This work attempted petrophysical analysis and rock physics modeling of the Traverse Limestone formation. Carbonate rocks have a very complex matrix due to different pore systems, which makes it difficult to predict their velocities. However, examining the lithology log to identify the minerals in the well help improve velocity prediction using rock physics modeling.

Mineral identification is achieved by studying the crossplots. The Neutron-density crossplot and the MID crossplot of UMA and DGA provide indications of the mineral components; however, the minerals in this system can be identified and seen more clearly through the PEF-Density crossplot, (especially dolomite and anhydrite). Using all of the crossplots mentioned above, an accurate result is determined. Identifying mineral components helps to estimate sonic velocities from different approaches.

Prediction of the P-wave velocity from Wyllie's Time Average equation was accurate in clean limestone rocks. In dolomitic formations though, the neutron log gives higher porosity on a limestone basis than the true porosity. If the porosity is not calculated through a neutron-density crossplot (or similar calculation), the porosity values obtained are too high. This gives a large error in the prediction of the P-wave velocity in dolomite using the typical application of Wyllie's Time equation. Sonic velocities are predicted from the Kuster-Toksöz equation and this works well when the mineral identification is accurate.

The relationship between the P-wave velocity and porosity also plays an essential role in the results of this study. We have obtained the best-fit aspect ratios for the calcite component in the limestone (the other mineral types, including quartz, dolomite, and anhydrite, have too low a porosity in our examples to provide best-fit aspect ratios). We have found that the aspect ratio for calcite is about 0.04. Other studies (e.g., Wang et al., 1991) have compared measured velocities directly with total porosity and classified pore shapes based on that aspect ratio (0.04). For our data this approach suggests a microcrack pore type. This determination of the pore types is consistent with the aspect ratios found from our application of the Kuster-Toksöz method.

5 Conclusion

The Traverse Limestone formation is composed of calcite, dolomite, quartz, anhydrite and a small amount of clay. In addition to the main limestone (calcite) fraction, some parts of the formation include significant amounts of dolomite, quartz and anhydrite. To determine these mineral components, the Neutron-density crossplots, MID crossplot of UMA and DGA crossplots, and the PEF crossplot were used. The mineral fractions determined from the crossplots were used to calculate the sonic velocities.

Sonic velocities were calculated from different approaches. The P-wave velocity was predicted using Wyllie's Time Average equation and the Kuster-Toksöz model. The two predicted values were then compared with the obtained P-wave velocity. The predicted P-wave velocity from Kuster-Toksöz model gave the best fit with the observed P-wave velocity. Furthermore, S-wave velocity was predicted from the Greenberg-Castagna equation and Kuster-Toksöz model. The predicted S-wave velocities gave similar results between the two equations, but the observed S-wave velocity was not recorded nor available for comparison.

The Wang (1991) modeling method was used by those authors to identify three different pore shapes using the velocities obtained from the Kuster-Toksöz equation. Under a similar assumption I created my own plot to show the relationship between porosity and the P-wave velocity obtained from the Kuster-Toksöz method. Combined with the aspect ratios that I obtained from the Kuster-Toksöz method and the Wang method, the conclusion is

that pore shapes generally tend to be microcracks when the formation includes a dolomite-anhydrite mix and a calcite-quartz mix.

6 References

Adcock, S. (1993), In search of the well tie; what if I don't have a sonic log?, The leading Edge, 12(12), 1161-1164, doi: 10.1190/1.1436929.

Brie, A., D. L. Johnson, and R. D. Nurmi (1985), Effect of spherical pores on sonic and resistivity measurements: Presented at SPWLA 26th Annual Logging Symposium.

Catacocinos, P. A, W.B. Harrison III, and P.A. Daniels, Jr. (1990), Structure, Stratigraphy, and Petroleum Geology of the Michigan Basin: Chapter 30: Part II. Selected

Analog Interior Cratonic Basins: Analog BasinRep., 40 pp.

Gassmann, F. (1951), Uber die Elastizität Poröser Medien: Vier. der Natur. Gesellschaft in Zürich 96, 1-23

Greenberg, M. L. and J. P. Castagna (1992), Shear-wave velocity estimation in porous rocks: Theoretical formulation, preliminary verification and applications: Geophysical Prospecting, 40, 195-209

Hasenmueller, N. R., and J. L. Bassett (1979), Maps of northern Indiana showing thicknesses of the Sunbury, Ellsworth, and Antrim Shales (New Albany Shale equivalents): Morgantown, W. Va., U.S. Dept. Energy, Morgantown Energy Technology Center, METC/EGSP Ser. No. 806 [1980].

Hill, R. (1952), The elastic behavior of a crystalline aggregate: Proceedings of the Physical Society, Section A, Volume 65, Issue 5, pp. 349-354 (1952).

Huntoon, J. E. and A. S. Wylie Jr. (2003), Log-curve amplitude slicing: Visualization of log data and depositional trends in the Middle Devonian Traverse Group, Michigan basin, United States, AAPG Bulletin, 87(4), 581-608, doi: 10.1306/12040201057.

Islam, N. (2011) Sonic log prediction in carbonates, Master's Thesis, Michigan Technological University, 2011.

Jordan J. R. and F. L. Campbell (1986) Well Logging II – Electric and Acoustic Logging: SPE Monograph Series, SPE, Dallas, TX

Keys, R. G. and S. Xu (2002), An approximation for the Xu-White velocity model, Geophysics, 67, 1406-1414.

Kuster, G. T., and M. N. Toksöz (1974), Velocity and attenuation of seismic waves in two-phase media: Part1: Theoretical formulation: Geophysics, Geophysics 39, 587-606.

Lilenthal, R.T. (1974), Subsurface Geology of Barry County, Michigan. Geological Survey, 18 pp, Lansing, Michigan.

Mavko G, T. Mukerji, and J. Dvorkin (2003), The rock physics handbook: Tools for seismic analysis in porous media. Cambridge University Press,

Miller, S. L. M. and R. R. Stewart (1990), Effect of lithology, porosity and shaliness on P- and S-wave velocities from sonic logs: Canadian Journal of Exploration Geophysics, Vol. 26, Nos 1&1, P. 94-103

Prison J. S. (1983), Geologic well log analysis. Gulf Publishing Company, Houston, Texas, 475 pp

Pringle, G. H. (1937), Progress Report Number Three, Geology of Arenac County. State of Michigan, 16 pp, Arena County.

Sams, M. and T. Focht (2013), An effective inclusion-based rock physics model for a sand-shale sequence: First Break, **31**, 61–71

Xu, S. and A. Payne (2009), Modeling elastic properties in carbonate rocks: The Leading Edge, 28, 66-74.

Xu, S., and R. E. White (1995), A new velocity model for clay-sand mixtures: Geophysical Prospecting, **43**, no. 1, 91–118

Wang Z, W. K. Hirsche and G. Sedgwick (1991), Seicmic velocities in carbonate rock: J. Canadian Petro. Tech., 30, 112-122

Wyllie, M. R. J., Gregory, A. R. & Gardner, G. H. F. 1958. An experimental investigation of factors affecting elastic wave velocities in porous media. Geophysics, 23: 459-93

7 Appendices

7.1 Appendix (I): Crossplots

7.1.1 MID of DGA and UMA Crossplot

For this crossplot, apparent grain density and apparent matrix volumetrix cross section with apparent total porosity are required to identify lithology using the data from density and litho-density log.

$$\mathrm{DGA} = \frac{\mathrm{RHOB} - \emptyset_t * \mathrm{RHOB}_f}{1 - \mathrm{PHIND}}$$

$$\mathrm{UMA} = \mathrm{PEF} * \frac{\mathrm{RHOB} + 0.1883}{1.0704}$$

DGA = Apparent Grain Density

$\emptyset_t$ = Apparent total porosity

UMA = Apparent matrix photo-electric volumetric cross section

PEF = Photoelectric absorption cross section

7.1.2 Additional Crossplots of Sampled Wells

Brandt Well:

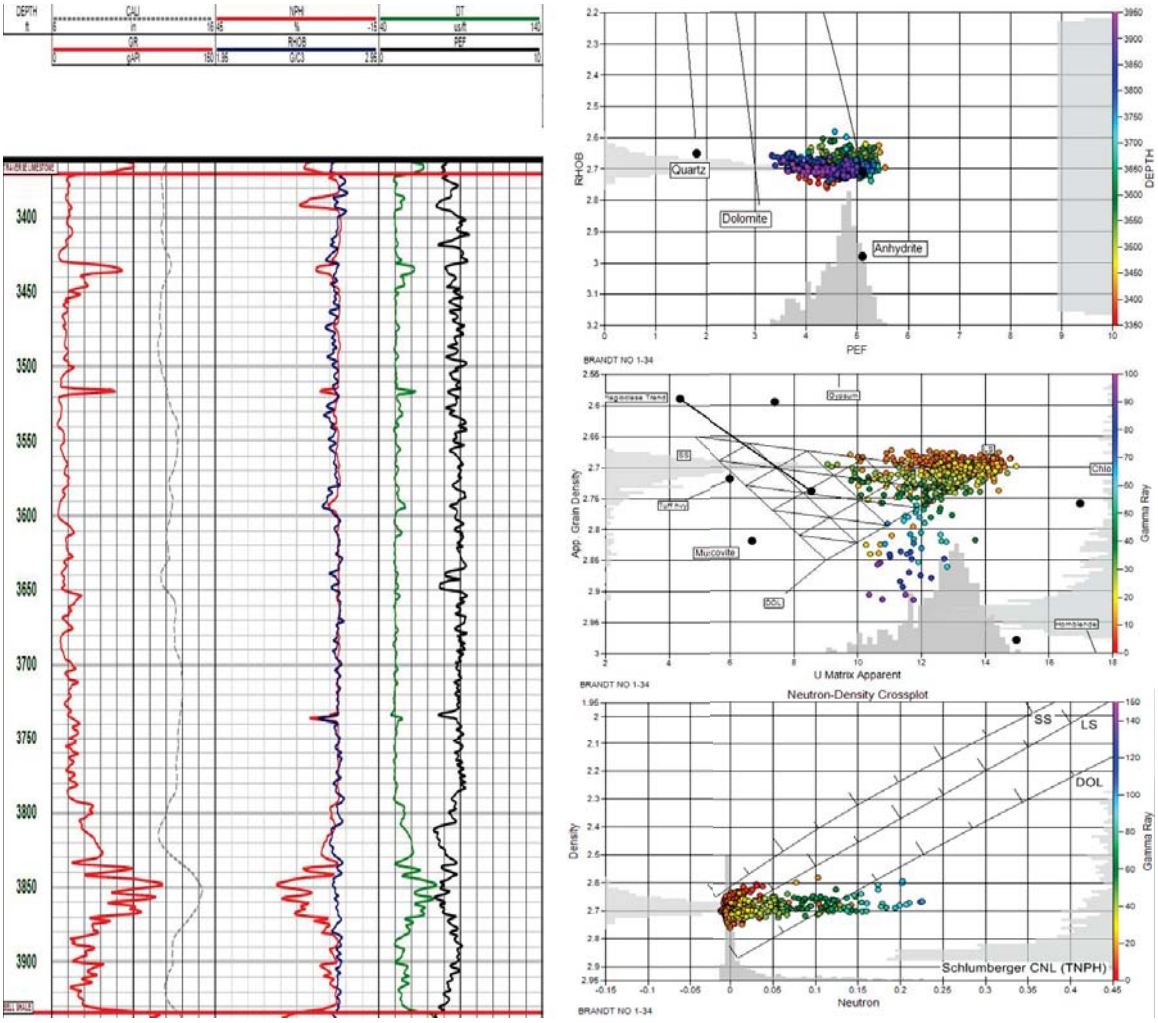

Figure 7.1. These log and crossplots were used to identify the mineralogy of the Traverse Limestone in the Brandt well. The gamma ray log indicates shale free formation until 3790 ft., and from 3790 ft. to the Bell Shale a small amount of shale presents. The neutron-density crossplot shows mostly a clean formation between lines of limestone and sandstone, and off those lines the scattering points are the result of the clay content. The MID of UMA and DGA crossplot indicates limestone and sandstone, and includes a small amount of shale. The Density-PEF crossplot could be interpreted that mixture is either dolomite or quartz. However, the previous crossplots eliminate dolomite as an option and limit the composition to limestone with quartz. The conclusion from the crossplots is that the formation presents limestone and sandstone.

Coates Well:

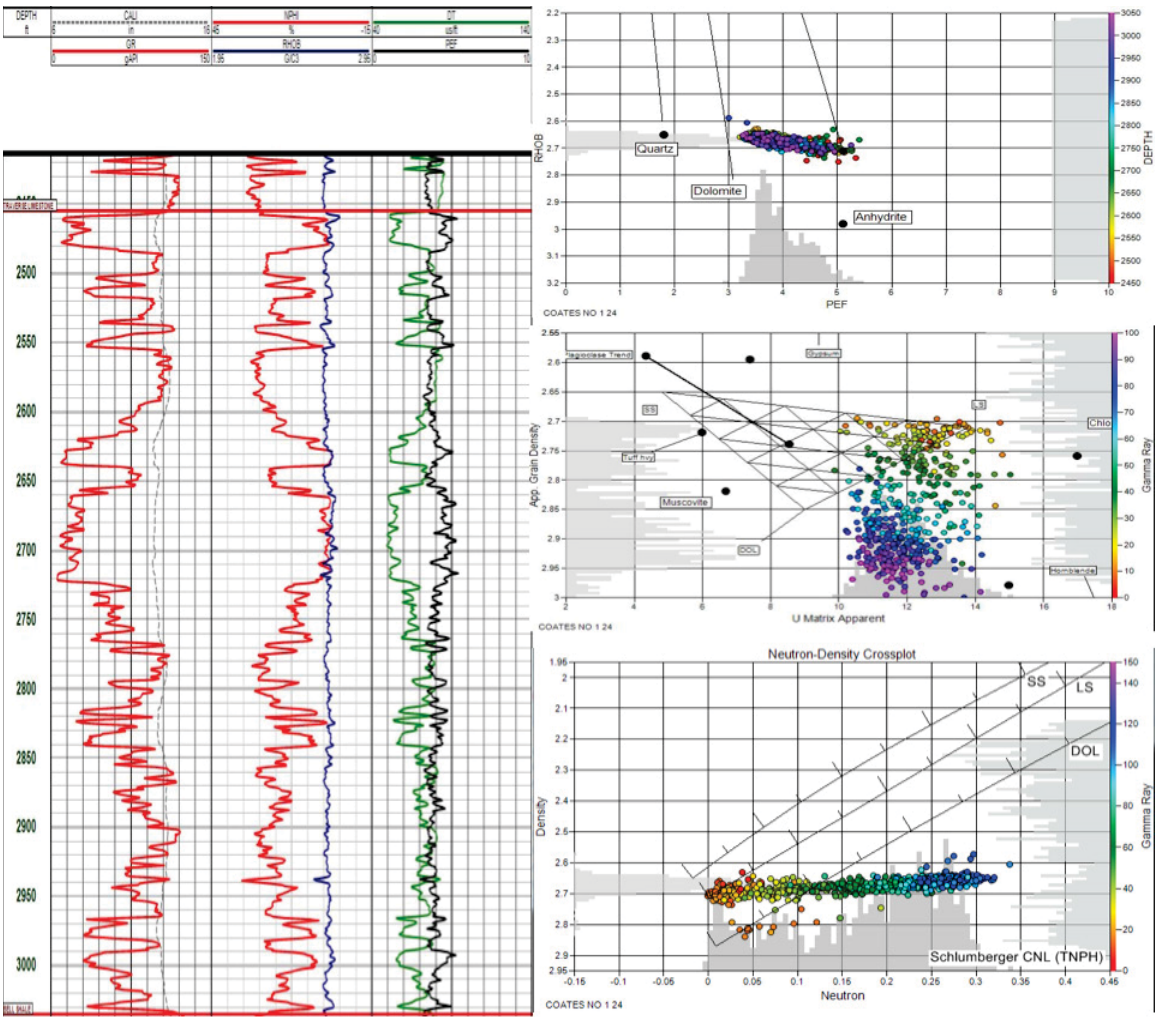

Figure 7.2. These log and crossplots were used to identify the mineralogy of the Traverse Limestone in the Coates well. The gamma ray log indicates a shaly formation. The neutron-density crossplot depicts a clean limestone with shaly formation. The MID of UMA and DGA crossplot indicates also limestone, and the data points located outside of the limestone region are the result of the shale content. The Density-PEF crossplot suggests a composition of calcite and quartz or a composition of calcite and dolomite. However, the additional crossplot remove the ambiguity of the composition by narrowing the possibility to quartz. The conclusion from all of the crossplots indicates that this formation is a shaly limestone.

Consumers Power Co Well:

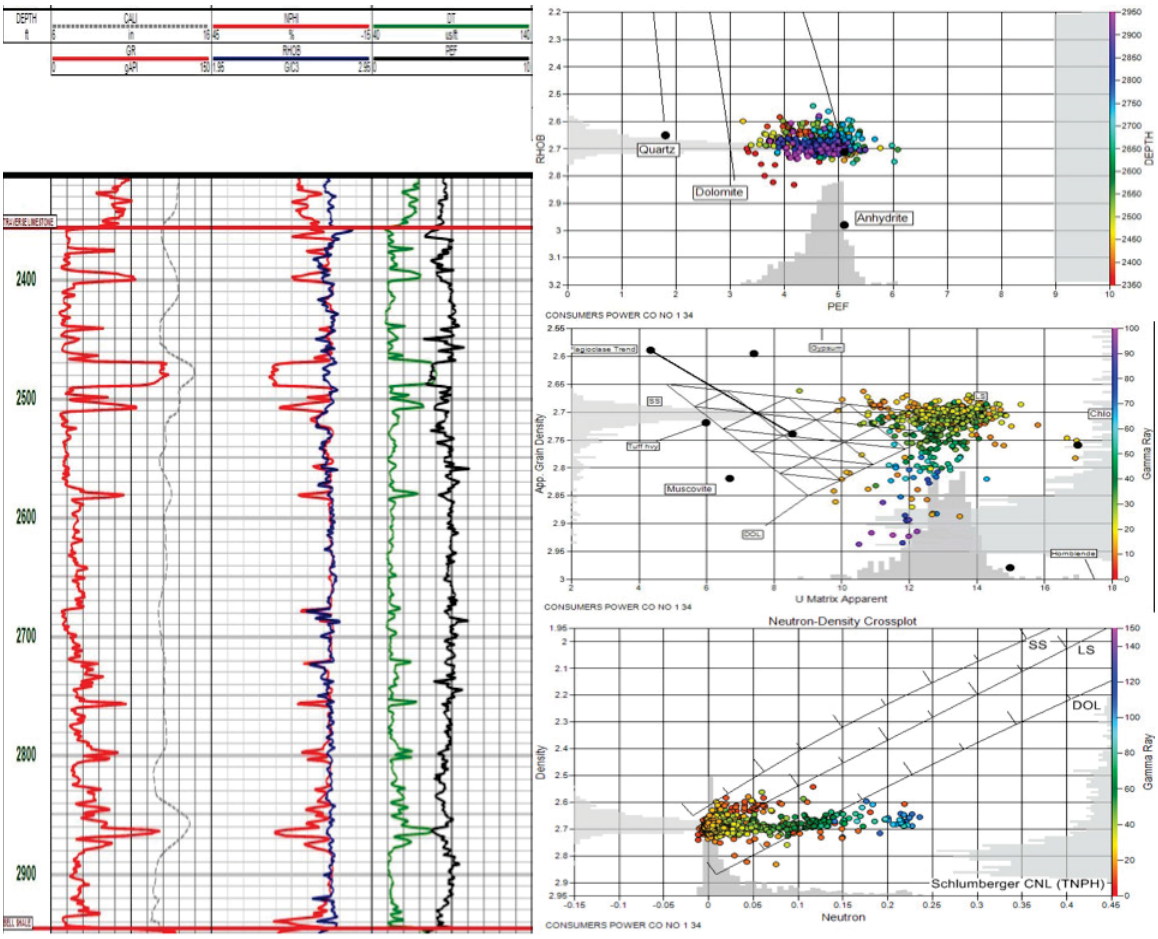

Figure 7.3. These log and crossplots were used to identify the mineralogy of the Traverse Limestone in the Consumers Power Co well. The gamma ray log illustrates a small amount of shale. The neutron-density crossplot represents a mixture of sandstone and limestone with a small amount of shale, and the data points located outside of the sandstone and limestone lines are the result of the clay content. The MID of UMA and DGA crossplot presences also limestone with a significant amount of sandstone. The Density-PEF crossplot indicates a mixture of calcite and quartz or calcite and dolomite. However, the other two crossplots eliminate dolomite as an option and narrow the composition to calcite with quartz, this well also presents limestone with quartz. The conclusion from all of the crossplots is that the composition of the formation is limestone and sandstone.

Gernaat Et Al Well:

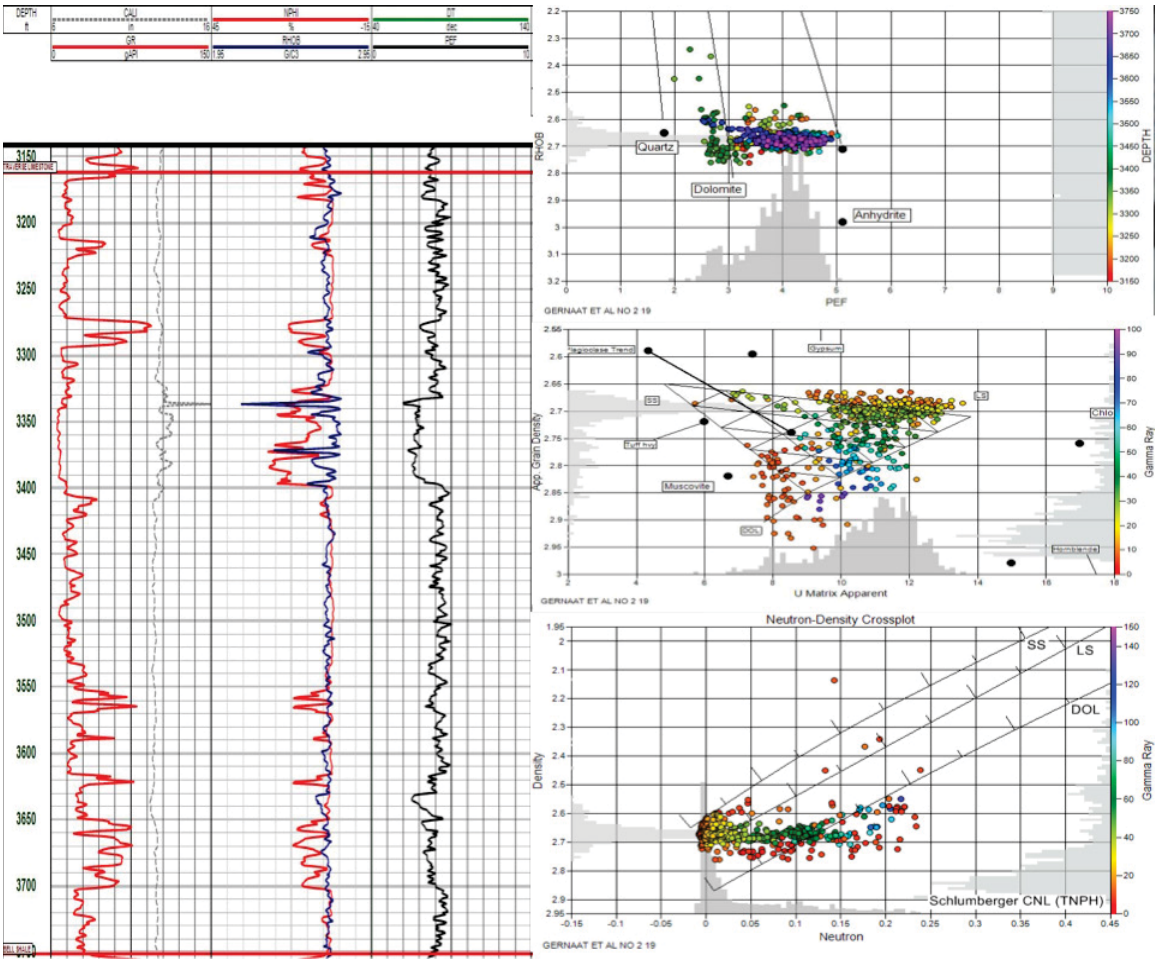

Figure 7.4. These log and crossplots were used to identify the mineralogy of Traverse Limestone at the Gernaat Et Al well. The gamma ray log indicates a small amount of shale. The neutron-density crossplot indicates shale free limestone, a significant amount of sandstone and a small amount of dolomite, and the remaining data points not located within these regions are the result of the clay content . The MID of UMA and DGA crossplot indicates also the mixture of limestone with a significant amount of sandstone and small amount of shale free dolomite. The Density-PEF crossplot shows a mixture of quartz, calcite, and a small amount of dolomite. The final result from all crossplots is that the Traverse Formation contains limestone, sandstone, and a small amount of dolomite.

Kennedy Well:

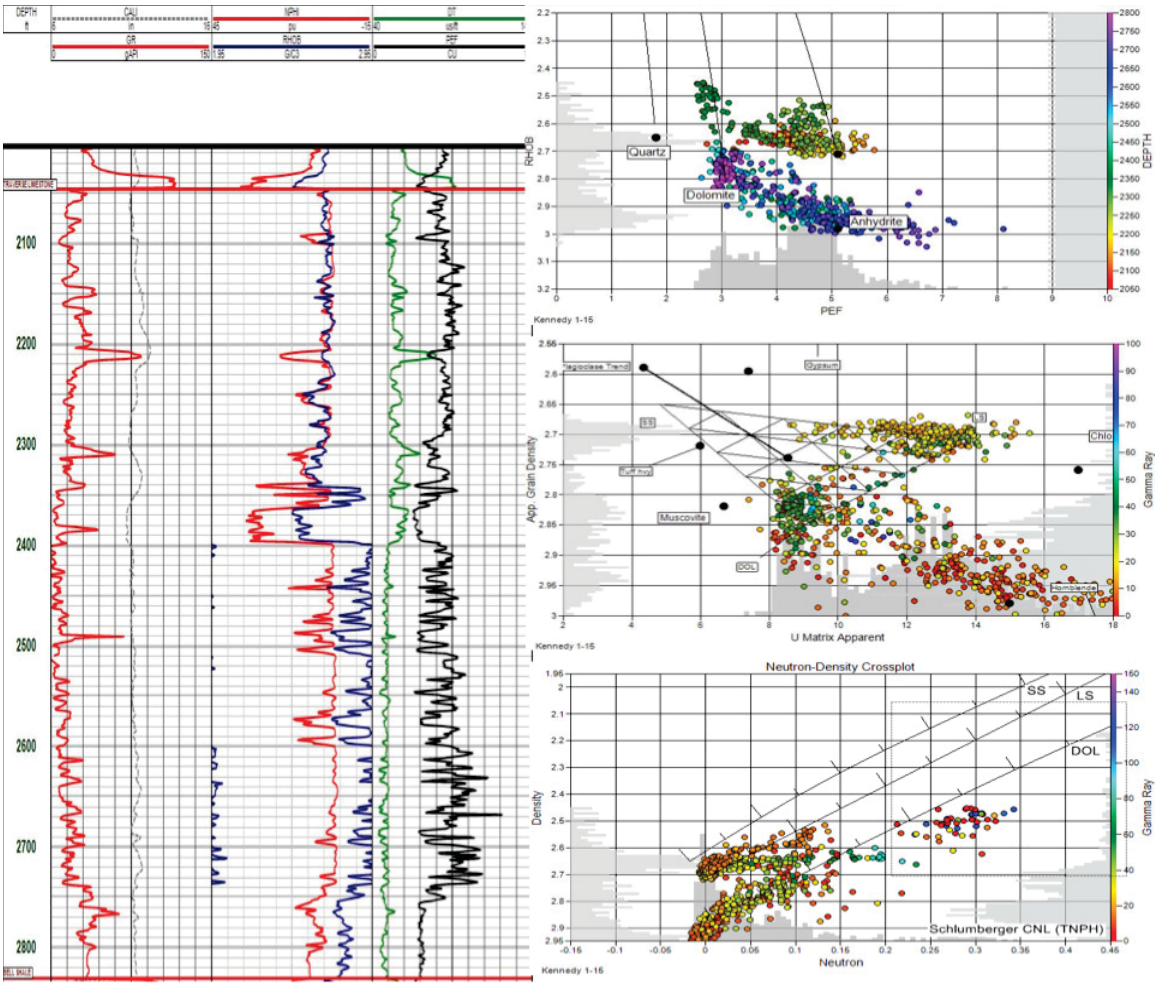

Figure 7.5. These log and crossplots were used to identify the mineralogy of the Traverse Limestone in the Kennedy well. The gamma ray log shows a shale free formation. The neutron-density crossplot indicates limestone with a significant amount of sandstone and dolomite. The MID of UMA and DGA crossplot represents a mixture of limestone with sandstone and dolomite and in the lower region there is a significant amount of anhydrite. The Density-PEF crossplot presents a mixture of calcite and quartz and a mixture of dolomite with a significant amount of anhydrite a various location of the Traverse Limestone. The Density_PEF crossplot indicates that the formation contains dolomite and anhydrite, underlying limestone and sandstone as depth is indicated in color.

Martin Well:

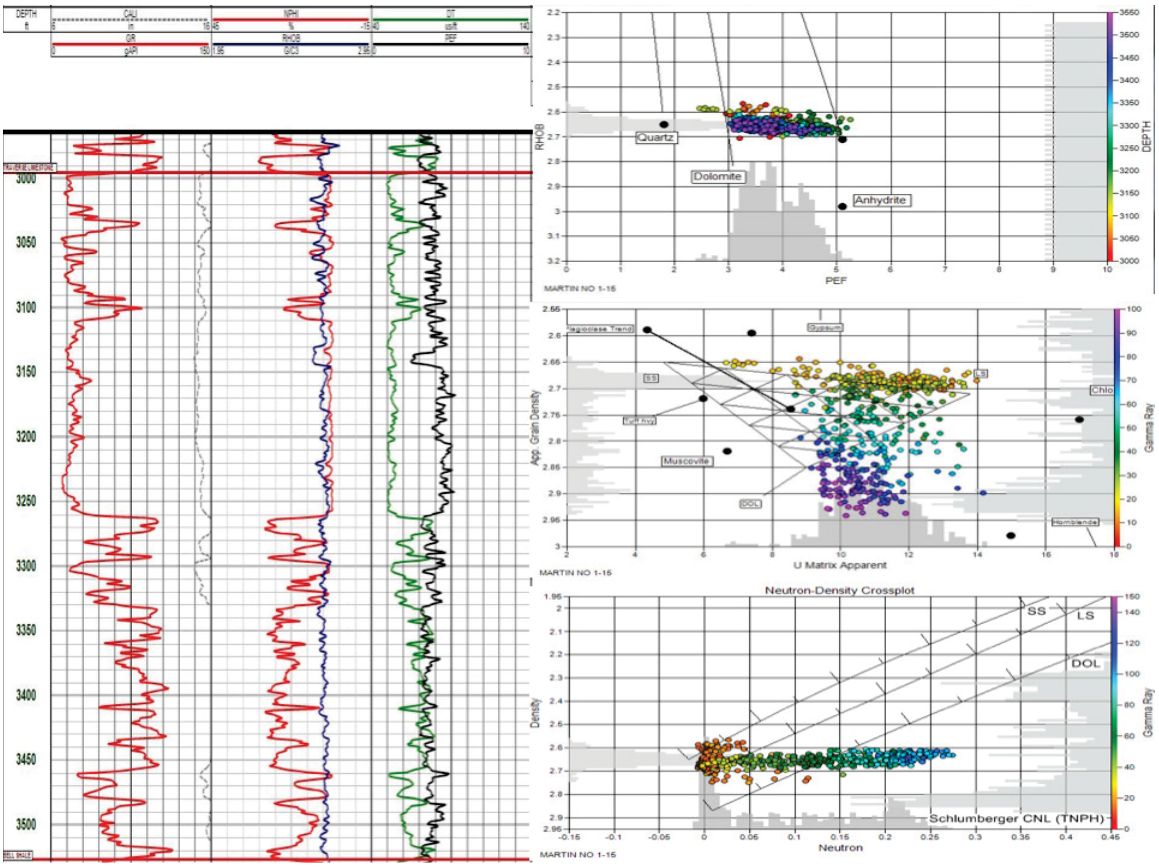

Figure 7.6. These log and crossplots were used to identify the mineralogy of the Traverse Limestone in the Martin well. The gamma ray log indicates a small amount of shale, with a significant amount of shale underlying the formation that indicates a small amount of shale. The neutron-density crossplot presents free shale formation of limestone with a significant amount of quartz, and the data points outside of the limestone and sandstone lines are the result of the clay content. The MID of UMA and DGA crossplot indicates limestone with sandstone with a significant amount of shale, and the data points located outside of the limestone and sandstone region as the result of the clay content as the neutron-density crossplot. The Density-PEF crossplot also shows a mixture of calcite and quartz. The final result of those crossplots is that the formation contains limestone with quartz with increasing shaliness in the deeper section.

Prevost Et Al Well:

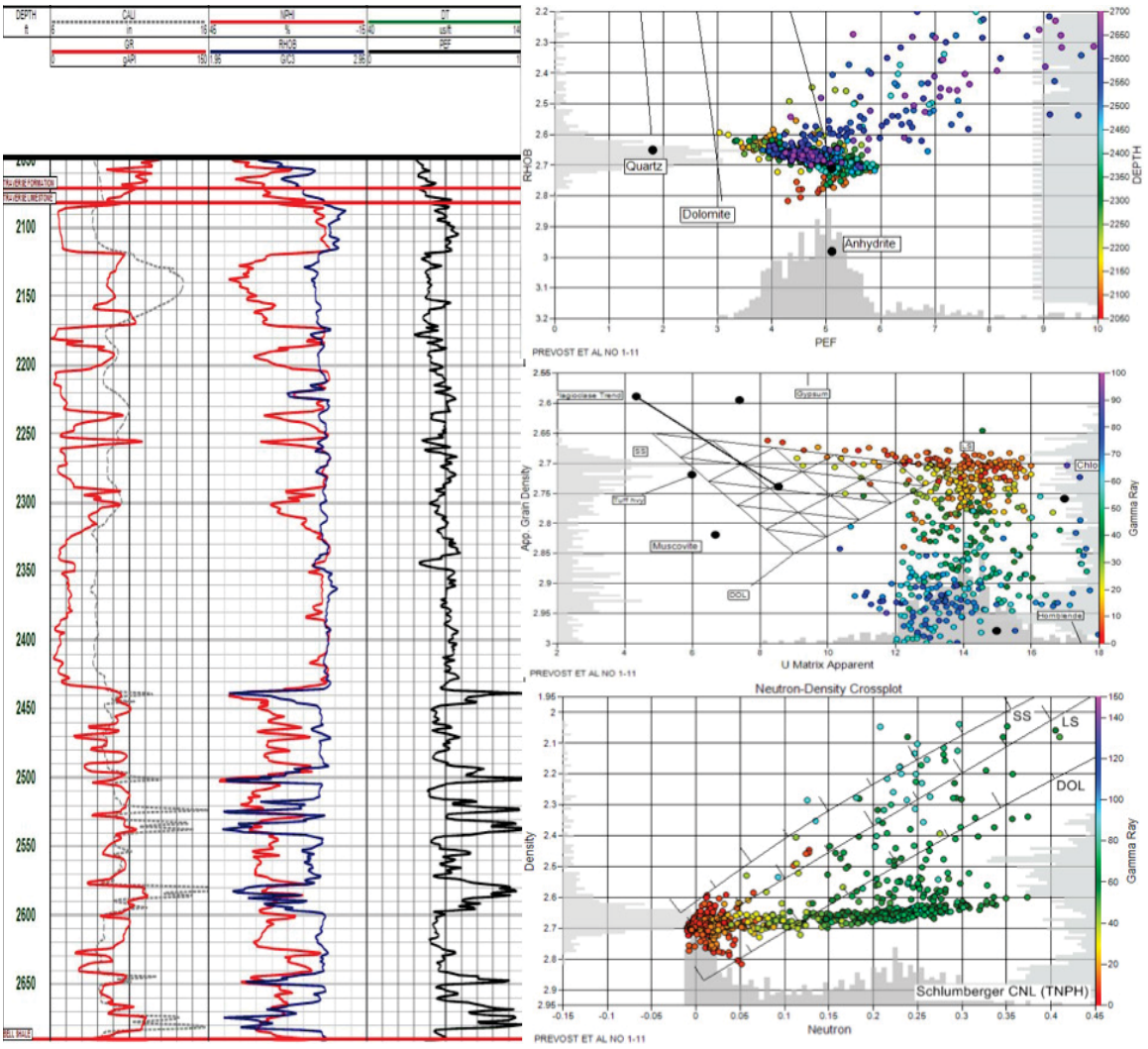

Figure 7.7. These log and crossplots were used to identify the mineralogy of the Traverse Limestone in the Prevost Et All well. The gamma ray log indicates a shaly formation. The neutron-density crossplot presents shale free formation between sandstone and limestone lines. The MID of UMA and DGA crossplot represents a mixture of limestone and sandstone and from the ternary diagrams the result of the shale content. The Density-PEF crossplot also gives a similar result as other two crossplot which presents calcite and quartz. The conclusion of the all the crossplots is that the formation contains limestone with significant amount of sandstone.

Snowplow Well:

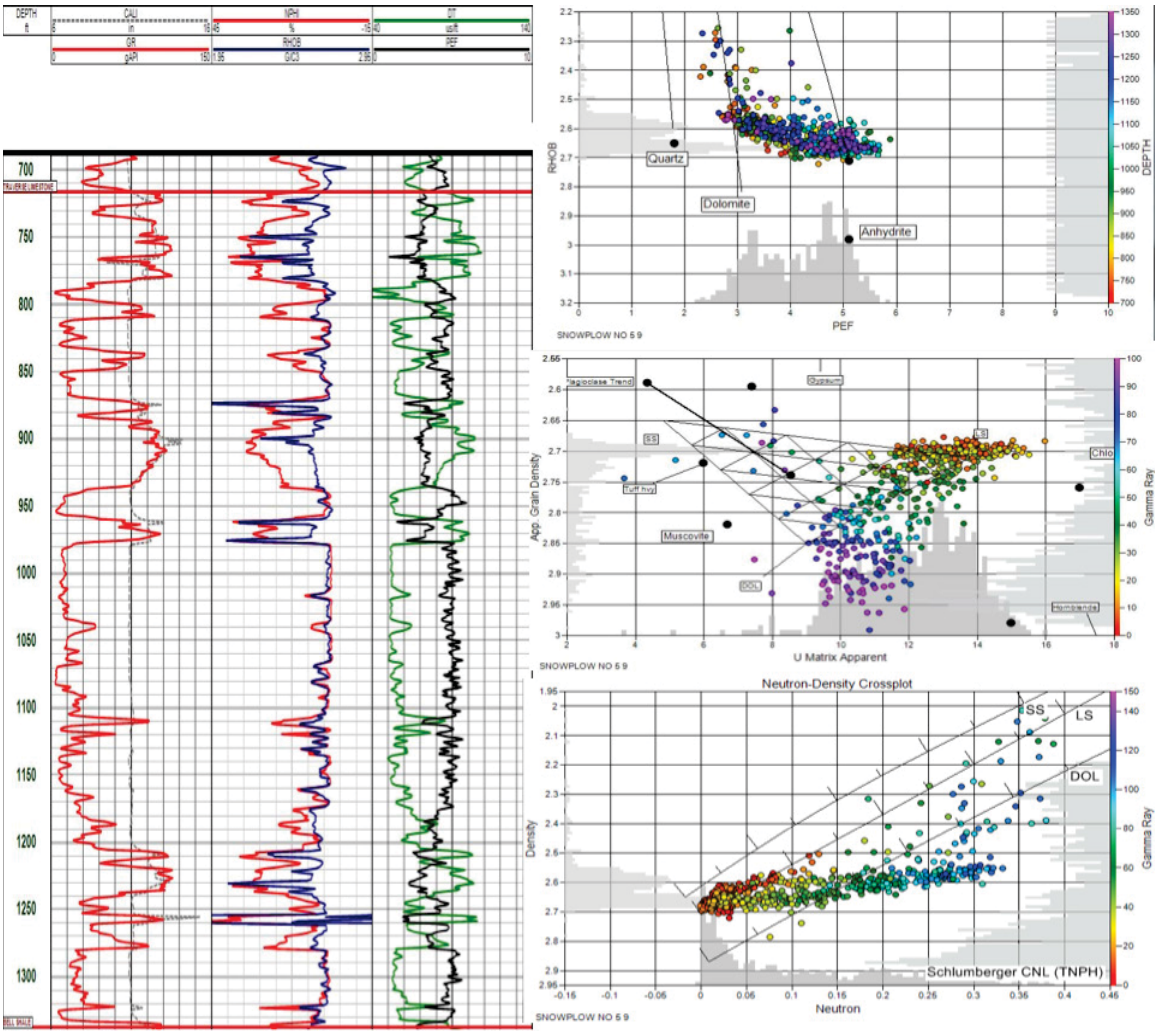

Figure 7.8. These log and crossplots were used to identify the mineralogy of the Traverse Limestone in the Snowplow well. The gamma ray log indicates a significant amount shale. The neutron-density crossplot presents clean limestone at a range of the depths with a small amount of sandstone, and also a significant amount of shale at the various depths. The MID of UMA and DGA crossplot shows limestone and it also presents a small amount of sandstone. The Density-PEF crossplot also indicates a mixture of quartz and calcite. The result of the crossplots is that at various depths the formation consists of clean limestone, clean limestone with a small amount of sandstone, and shaly formation.

Visser Well:

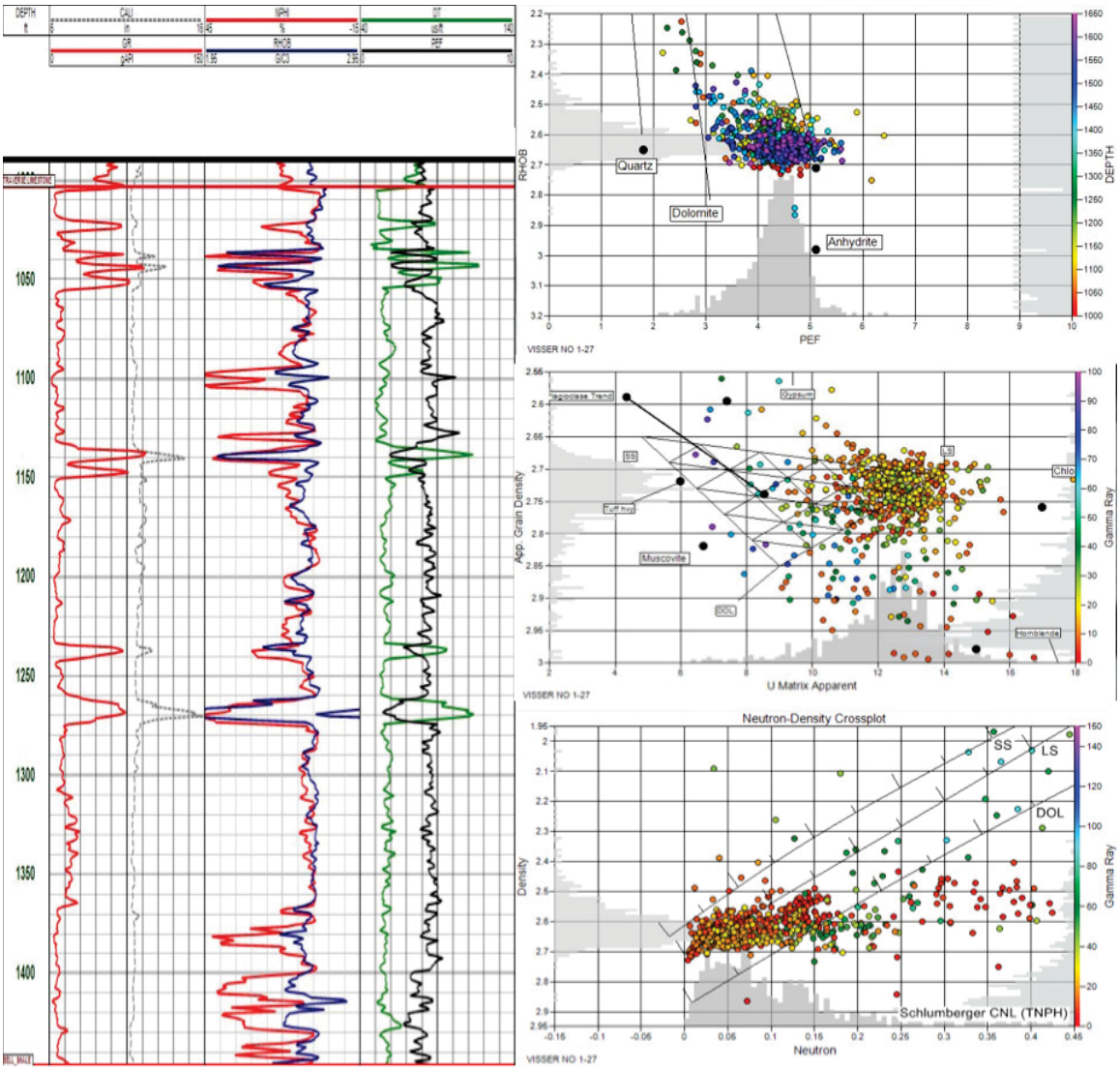

Figure 7.9. These log and crossplots were used to identify the mineralogy of the Traverse Limestone in the Visser well. The gamma ray log indicates a small amount of shale. The neutron-density crossplot presents clean limestone and the data points outside of the limestone region is the result of a small amount of shale content. The MID of UMA and DGA crossplot shows also limestone. The Density-PEF crossplot interpretation present clean calcite. The conclusion of the crossplots is that the formation consists of clean limestone with small amounts of shale at various depths.

Haroutunian Unit Well:

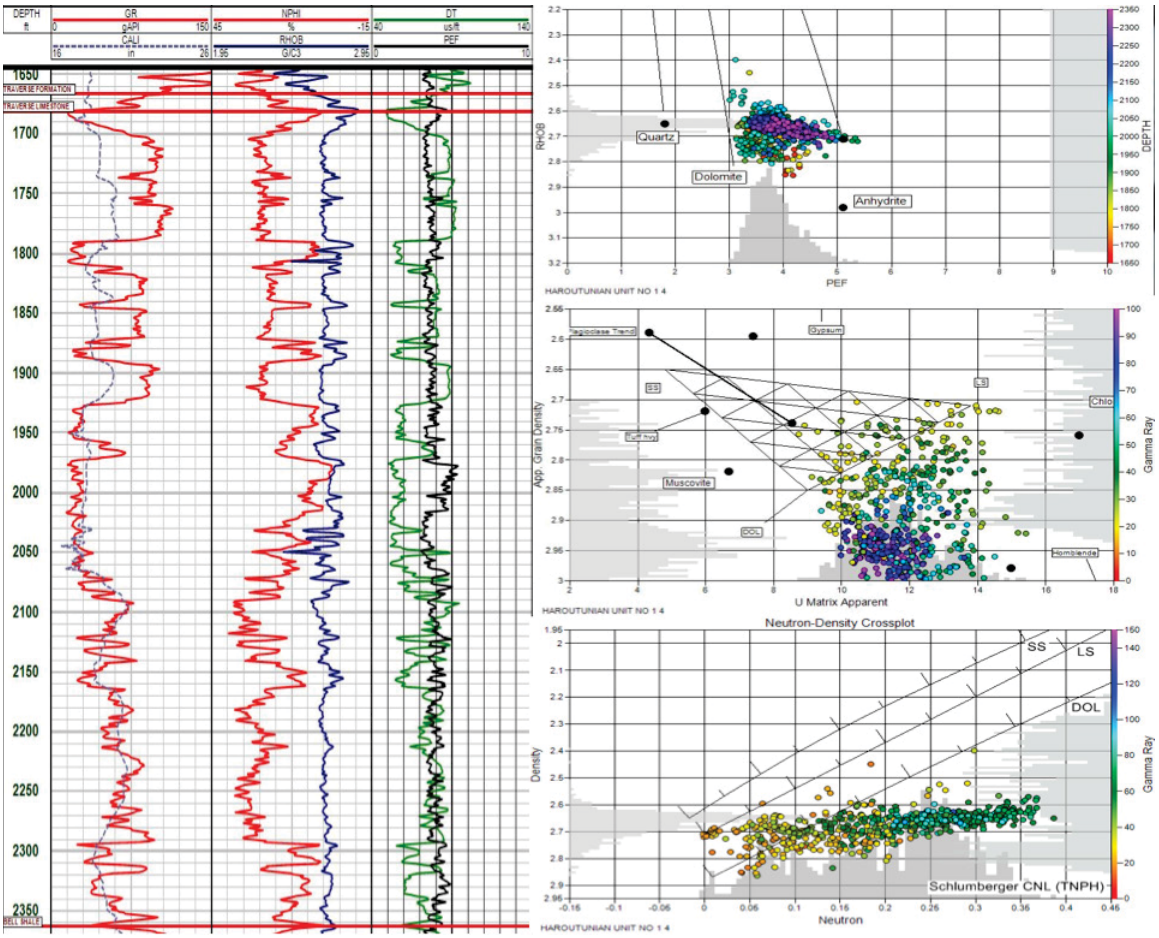

Figure 7.10. These log and crossplots were used to identify the mineralogy of the Traverse Limestone in the Haroutunian Unit well. The gamma ray log indicates a shaly formation, and the caliper log gives some error where the formation has shale content. The neutron-density crossplot presents clean limestone and a small amount of dolomite, while the other data points the outside of the lines of limestone and dolomite is result of the large shale content. The MID of UMA and DGA crossplot shows also limestone with a small amount of dolomite. The Density-PEF crossplot interprets shale free limestone and dolomite, and scattered data points because of shale, which is demonstrated on the depth axis. The conclusion of the crossplots is the formation presents clean limestone and dolomite with a significant amount of shale at the majority of the depth ranges.

Huber Well:

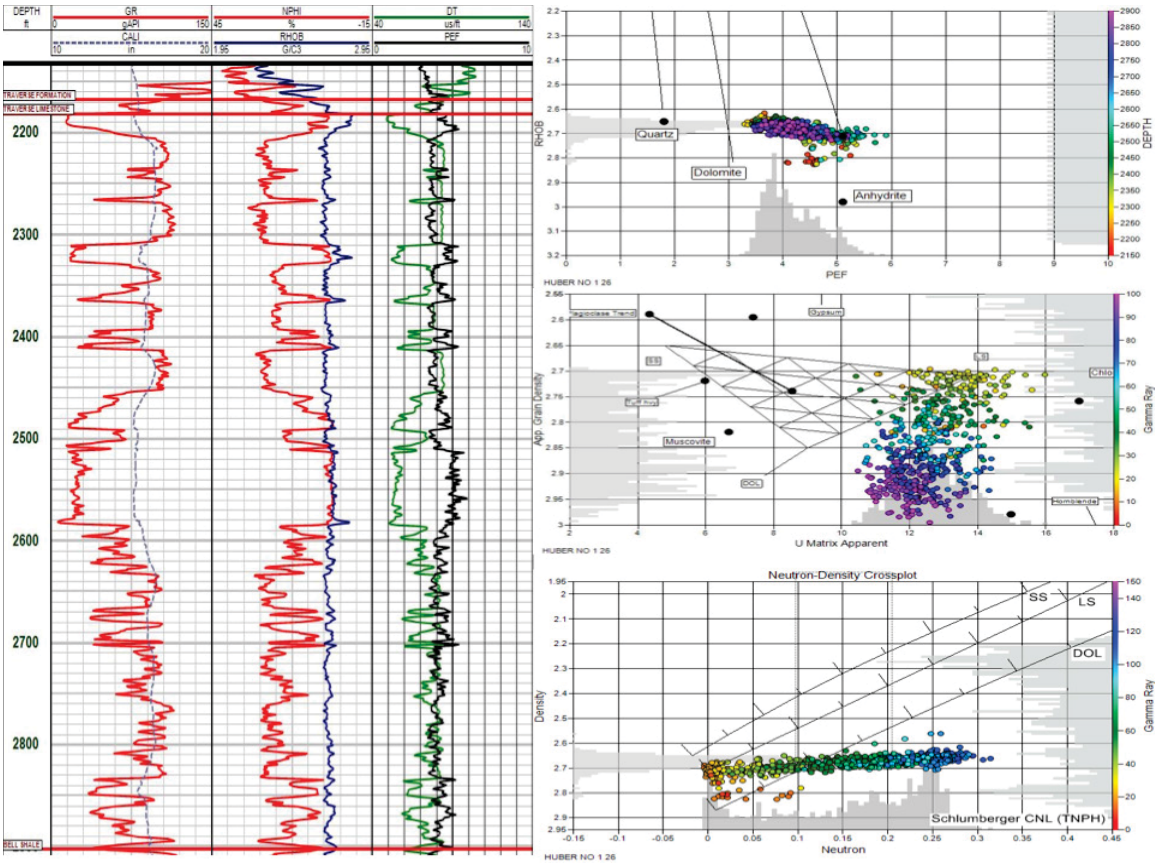

Figure 7.11. These log and crossplots were used to identify the mineralogy of the Traverse Limestone in the Huber well. The gamma ray log indicates a shaly formation. The neutron-density crossplot presents clean limestone and insignificant dolomite, while the other scattered data points are out of the limestone region as a result of the large shale content. The MID of UMA and DGA crossplot shows also limestone with a significant amount of shale. The Density-PEF crossplot interprets shale free limestone and dolomite, and scattered data points because of shale, which is depicted on the depth axis. The conclusion of the crossplots is that the formation presents clean limestone and a very small amount of dolomite with a significant amount of shale at the majority of the depth ranges.

7.2 Appendix (II): Root-Mean-Square (RMS) Error Calculation

$$RMS = \sqrt{\frac{\sum_{i=1}^{n}(\ddot{y}_i - y_i)^2}{n}}$$

n = Depth

ÿ = Predicted values

y = Observed values

In this study, the depth range is selected to calculate RMS error for over the depth ranges that are mostly quartz and calcite and that are mostly dolomite and anhydrite.

7.3 Appendix (III): Lithology Log

The lithology log was made by using the mineral components derived from the crossplots. The formation includes a small amount of shale which was ignored in the calculations. The mineral fractional volume of each of the minerals was generally estimated from the ternary diagram from the MID of DGA and MID crossplot for each depth with cross checking with the other crossplots. An example of a small depth range of the formation is shown in Figure 7.13, with a table that shows the fractional volume by depth. This example is taken from the Kennedy well, whose logs and crossplots are shown in Figure 3.2.5-11.

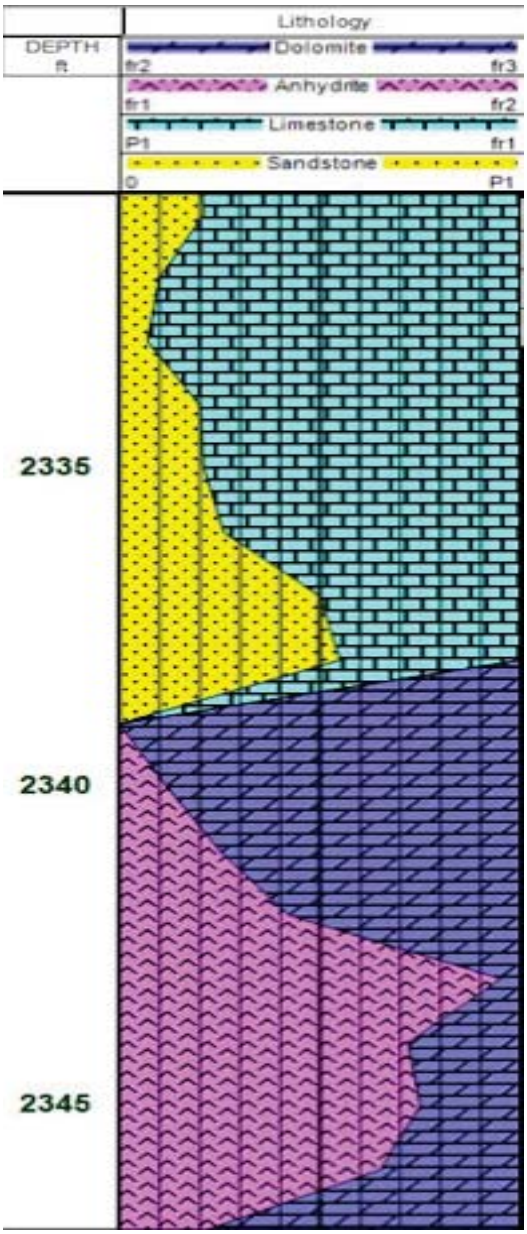

Depth	Fraction of Quartz	Fraction of Calcite	Fraction of Anhydrite	Fraction of Dolomite
2330	0.20	0.80	0.00	0.00
2331	0.21	0.79	0.00	0.00
2332	0.10	0.90	0.00	0.00
2333	0.07	0.93	0.00	0.00
2334	0.20	0.80	0.00	0.00
2335	0.21	0.79	0.00	0.00
2336	0.26	0.74	0.00	0.00
2337	0.50	0.50	0.00	0.00
2338	0.55	0.45	0.00	0.00
2339	0.00	0.00	0.00	1.00
2340	0.00	0.00	0.12	0.88
2341	0.00	0.00	0.25	0.75
2342	0.00	0.00	0.42	0.58
2343	0.00	0.00	0.95	0.05
2344	0.00	0.00	0.72	0.28
2345	0.00	0.00	0.75	0.25
2346	0.00	0.00	0.65	0.35
2347	0.00	0.00	0.19	0.81
2348	0.00	0.00	0.00	1.00
2349	0.00	0.00	0.30	0.70
2350	0.00	0.00	0.67	0.33

Figure 7.13. This figure shows an example of the lithology log of the Kennedy well and the table of the fraction of the minerals.

7.4 Appendix (IV): The Kuster-Toksöz Model (1974)

The Kuster-Toksöz Model uses a combination of the porosities, the aspect ratios, and the elastic properties of the different fractions in the matrix to calculate the sonic velocities of the matrix. For Kuster-Toksöz equation, total porosity was calculated from neutron porosity log and density log, and the fractions of the minerals were calculated from the crossplots.

$$\emptyset_t = \emptyset_m + \emptyset_c$$

$$\emptyset_m = V_m * \frac{\emptyset_t}{1 - \emptyset}$$

$$\emptyset_c = V_c * \frac{\emptyset_t}{1 - \emptyset_t}$$

$\emptyset_m =$ The porosity of the matrix

$\emptyset_c =$ The porosity of the clay

V_m = The volume of the matrix

V_c = The volume of the clay

$$\theta = \frac{\alpha}{(1-\alpha)^{3/2}}\left[\cos^{-1}(\alpha) - \alpha\sqrt{1-\alpha^2}\right]$$

$$g = \frac{\alpha^2}{1-\alpha^2}(3\theta - 2)$$

$$R = \frac{3\mu}{3K + 4\mu}$$

$$B = \frac{1}{3}\left(\frac{K'}{K} - \frac{\mu'}{\mu}\right)$$

$$A = \frac{\mu'}{\mu} - 1$$

$$F_1 = 1 + A\left[\frac{3}{2}(g+\theta) - R\left(\frac{3}{2}g + \frac{5}{2}\theta - \frac{4}{3}\right)\right]$$

$$F_2 = 1 + A\left[1 + \frac{3}{2}(g+\theta) - \frac{R}{2}(3g+5\theta)\right] + B(3-4R)$$
$$+ \frac{A}{2}(A+3B)(3-4R)[g+\theta-R(g-\theta+2\theta^2)]$$

$$F_3 = 1 + \frac{A}{2}\left[R(2-\theta) - R\left(\frac{3}{2}g + \frac{5}{2}\theta - \frac{4}{3}\right)\right]$$

$$F_4 = 1 + \frac{A}{4}[3\theta + g - R(g-\theta)]$$

$$F_5 = A\left[R\left(g+\theta-\frac{4}{3}\right) - g\right] + B\theta(3-4R)$$

$$F_6 = 1 + A[1 + g - R(\theta+g)] + B(1-\theta)(3-4R)$$

$$F_7 = 2 + \frac{A}{4}[9\theta + 3g - R(5\theta+3g)] + B\theta(3-4R)$$

$$F_8 = A\left[1 - 2R + \frac{g}{2}(R-1) + \frac{\theta}{2}(5R-3)\right] + B(1-\theta)(3-4R)$$

$$F_9 = A[g(R-1) - R\theta] + B\theta(3-4R)$$

$$T_1 = \frac{3F_1}{F_2}$$

$$T_2 = \frac{2}{F_3} + \frac{1}{F_4} + \frac{F_4 * F_5 + F_6 * F_7 - F_8 * F_9}{F_2 * F_4}$$

$$K_e = \frac{K + 1.333 * \mu * (K' - K) * T_1}{\frac{1 - (K' - K) * T_1}{3 * K + 4 * \mu}}$$

$$\mu_e = \frac{\mu + \mu * T_2 * (9K + 8\mu) * (\mu' - \mu)}{\frac{1 - 6 * (K + 2 * \mu) * T_2 * (\mu' - \mu)}{25 * \mu * (3 * K + 4 * \mu)}}$$

$$V_p = \sqrt{\frac{K_e + 1.333 * \mu_e}{RHOB}}$$

$$V_s = \sqrt{\frac{\mu_e}{RHOB}}$$

K = The bulk moduli of the matrix

K′= The bulk moduli of the fluid

μ = The shear moduli of the matrix

μ' = The shear moduli of the fluid

K_e = The effective bulk moduli

μ_e = The effective shear moduli

V_p = P-wave velocity

V_s = S-wave velocity

α = Aspect ratio of the inclusion